Arabian Journal for Science and Engineering
https://doi.org/10.1007/s13369-025-11011-1

RESEARCH ARTICLE - SPECIAL ISSUE - AJSE 50TH ANNIVERSARY: FIVE DECADES OF SCIENTIFIC EXCELLENCE

Oxidative Band Alignment Shift in AgO- and ZrO_2-Modified Fibrous Silica Iron for Dual-Pollutant Photocatalysis

Nur Izzati Hannani Hazril[1] · Aishah Abdul Jalil[1,2] · Nurul Sahida Hassan[1] · Liew Shi Yan[1] · Muhammad Hakimi Sawal[1] · Nik Muhammad Izzudin[1] · Muhammad Hafizuddin Mohd Sofi[1] · Nurfatehah Wahyuny Che Jusoh[3] · Faiz Arith[4] · Sudiyarmanto Sudiyarmanto[5]

Received: 18 November 2025 / Accepted: 8 December 2025

Abstract

Industrial wastewater treatment remains a pressing challenge owing to the coexistence of hazardous heavy metals and persistent organic dye contaminants that resist conventional remediation approaches. In this work, a fibrous silica iron (FSFe) catalyst was successfully incorporated with metal oxides (AgO, ZrO_2) via a microemulsion-assisted electrolysis method, leading to a uniform dispersion of the metal oxides across the fibrous framework. Among the synthesized composites, AgO/FSFe exhibited superior photocatalytic activity in dual removal of hexavalent chromium (Cr(VI)) and methyl orange (MO) compared to that of ZrO_2/FSFe and pristine FSFe. Structural characterization confirmed the successful formation of Si–O–M bonds in AgO/FSFe and the electron transfer from AgO to FSFe, indicating strong interfacial interactions. This improvement results from an oxidative shift in the conduction and valence bands, which enables optimal band alignment and a stable *p–n* heterojunction structure, thereby minimizing electron–hole recombination, as supported by photoluminescence (PL), electrochemical impedance spectroscopy (EIS), and Mott–Schottky analyses. Scavenger experiments revealed that photogenerated electrons were the main contributors to Cr(VI) reduction, whereas ·OH radicals dominated MO degradation. Under optimized conditions (pH 3, catalyst dosage 0.25 g L^{-1}, initial concentrations of 20 mg L^{-1} Cr(VI) and 10 mg L^{-1} MO), the 10AgO/FSFe catalyst achieved simultaneous removal efficiencies of 64.37% for Cr(VI) and 99.45% for MO while maintaining its performance over five successive cycles, outperforming the photolysis and single-pollutant systems. Furthermore, the catalyst demonstrated versatility by effectively degrading additional organic dyes. This structure enhances charge separation and enables the simultaneous removal of heavy metals and organic pollutants, establishing AgO/FSFe as a durable and sustainable wastewater photocatalyst.

Keywords Oxidative Band Alignment · AgO · ZrO_2 · Modified Fibrous Silica Iron · Dual-Pollutant · Photocatalysis

1 Introduction

Water pollution remains an urgent and escalating environmental issue, intensified by anthropogenic activities, especially industrialization, that discharge complex pollutants, such as heavy metals and organic compounds, into

✉ Aishah Abdul Jalil
r-aishahj@utm.my

[1] Faculty of Chemical and Energy Engineering, Universiti Teknologi Malaysia, 81310 Johor Bahru, Johor, Malaysia

[2] Center of Hydrogen Energy, Institute of Future Energy, Universiti Teknologi Malaysia, 81310 Johor Bahru, Johor, Malaysia

[3] Department of Chemical and Environmental Engineering, Malaysia-Japan International Institute of Technology, Universiti Teknologi Malaysia Kuala Lumpur, 54100 Kuala Lumpur, Malaysia

[4] Faculty of Electronic and Computer Technology and Engineering, Universiti Teknikal Malaysia Melaka, Hang Tuah Jaya, 76100 Durian Tunggal, Melaka, Malaysia

[5] Research Centre for Chemistry, National Research and Innovation Agency (BRIN), Building 452 Kawasan Sains dan Teknologi BJ. Habibie Serpong, South Tangerang, Banten 15314, Indonesia

Published online: 05 January 2026

aquatic ecosystems. Industrial effluents, particularly from leather tanning, electroplating, paper manufacturing, textile dyeing, and metal finishing industries, frequently contain contaminants of emerging concern (CECs) such as hexavalent chromium (Cr(VI)) and methyl orange (MO) [1–4]. Inadequate treatment and improper disposal of these pollutants in non-compliance with water quality standards present serious risks to aquatic organisms and hinder water purification efforts. The pronounced harmfulness of both pollutants in water systems contributes to considerable health hazards, including dermal and ocular irritations, respiratory complications, and gastrointestinal diseases, while simultaneously threatening environmental integrity [5–8]. Consequently, a wide range of remedial approaches, such as biological treatment [9], electrolysis [10], and adsorption [11], have been extensively investigated for the concurrent removal of heavy metals and organic contaminants from wastewater. Nonetheless, these techniques face significant limitations, including high operational costs, susceptibility to fouling, complex post-treatment requirements, and the potential to produce more complex pollutants than the initial contaminants [12–14].

Advanced oxidation processes (AOPs), recognized as a green chemistry approach, offer mild operating conditions, high oxidation efficiency, and excellent stability, making them valuable for the simultaneous removal of multiple pollutants, such as Cr(VI) and methyl orange (MO) [15–18]. In recent years, semiconductor-based photocatalysts such as titanium dioxide (TiO_2), cadmium sulfide (CdS), zinc oxide (ZnO), and iron oxide (Fe_2O_3) have been extensively studied for this purpose [19–22]. However, unmodified semiconductors often exhibit poor visible-light absorption and severe electron–hole recombination, limiting their practical performance. To overcome these challenges, integrating semiconductors into fibrous silica frameworks has gained increasing attention. The fibrous silica morphology, composed of interwoven fibers and small to medium pores, provides a high surface area, abundant defect sites, and efficient charge-transfer pathways, enhancing photocatalytic activity [23–25]. Among these, fibrous silica iron (FSFe) has shown promise for visible-light-driven simultaneous reduction of Cr(VI) and degradation of MO, particularly when assisted by hydrogen peroxide (H_2O_2) [26]. The photo-Fenton reactions between H_2O_2 and Cr(VI) generate hydroxyl radicals that aid in pollutant degradation; however, excessive radicals may reoxidize Cr(III), thereby reducing overall efficiency. Therefore, further modification of FSFe through band gap engineering and heterojunction formation is crucial to achieve stable and efficient dual-pollutant remediation.

Doping photocatalysts with metal oxides onto suitable supports has proven to be an effective strategy for enhancing photocatalytic efficiency [27–29]. Our research group has developed several fibrous silica metal oxide photocatalysts using electrochemical and wet impregnation methods, demonstrating excellent potential for pollutant removal [30–32]. For example, fibrous silica zirconia (FSZr) modified with silver oxide (AgO) or zinc oxide (ZnO) exhibited superior performance in reducing Cr(VI) and degrading organic pollutants through type I and *p–n* heterojunction formation, respectively [30, 32]. Constructing heterojunctions with stable metal oxides such as AgO and ZrO_2 is particularly promising, as their tunable electronic structures and strong oxidation potentials contribute to durable photocatalytic activity. In general, *p–n* heterojunctions generate strong internal electric fields that enhance charge separation, while *n–n* heterojunctions depend primarily on band alignment [11, 28, 33–35]. However, limited studies have compared these systems beyond interfacial charge behavior. Despite significant progress, most band gap engineering research still targets single-pollutant systems dominated by photooxidation at the valence band, with minimal attention given to photoreduction at the conduction band [36–40]. This issue is critical since Cr(VI) reduction to Cr(III) remains challenging due to its high redox potential and aqueous stability [41]. Therefore, understanding how band alignment and oxidative band gap modulation influence both photoreduction and photooxidation is crucial for developing efficient dual-pollutant remediation systems.

Inspired by previous studies, fibrous silica iron (FSFe) composites doped with various metal oxides (AgO, ZrO_2) were systematically synthesized to tailor band alignment, facilitate efficient charge transfer, and suppress electron–hole recombination. This study emphasizes the significance of investigating pH-dependent behavior under multi-pollutant conditions while evaluating pollutant concentrations and radical scavengers to elucidate the photocatalytic removal mechanisms of Cr(VI) and MO, relying solely on catalyst modification without the use of additional solvents. The developed system demonstrates the potential of FSFe-based photocatalysts as an effective and sustainable platform for the simultaneous removal of heavy metals and organic contaminants. Despite extensive research on photocatalytic materials, no prior study has comprehensively explored the synergistic influence of oxidative band gap shifts on the remediation of dual pollutant. Addressing this gap, the present work introduces oxidative band alignment engineering as a strategic approach to achieve balanced photooxidation and photoreduction processes, thereby advancing the design of efficient photocatalysts for real wastewater treatment applications.

2 Experimental

2.1 Materials

Butanol ($C_4H_{10}O$), cetyltrimethylammonium bromide (CTAB, $C_{19}H_{42}BrN$), toluene (C_7H_8), and tetraethyl orthosilicate (TEOS, $SiC_8H_{20}O_4$) were supplied by Merck (Darmstadt, Germany). Urea (CH_4N_2O), iron (III) oxide (Fe_2O_3), potassium carbonate (K_2CO_3), potassium chlorate ($KClO_3$), and sodium hydrogen carbonate ($NaHCO_3$) were obtained from Sigma-Aldrich (St. Louis, USA). The silver (Ag), zirconium (Zr), platinum (Pt) plates were obtained from Nilaco Metal (Tokyo, Japan). The tetraethylammonium perchlorate, TEAP ($C_8H_{20}ClNO_4$), was used as electrolyte and prepared according to previous literature [42]. For the target pollutants, potassium dichromate ($K_2Cr_2O_7$) was used as source of Cr(VI) from Emorg (Selangor, Malaysia), while MO was from Qrec Asia (Selangor, Malaysia). Hydrochloric acid (HCl) and sodium hydroxide (NaOH) from Sigma-Aldrich (St. Louis, USA) were used as calibration pH for the pollutants.

2.2 Synthesis of FSFe and m/FSFe Catalysts

The FSFe catalysts were synthesized through a microemulsion approach, as delineated by a previous researcher [26]. The procedure commenced with the blending of urea (15 g), toluene (600 mL), CTAB (15 g), and distilled water (700 mL) homogenously in a 2-L Teflon at ambient temperature. Next, Fe_2O_3 (5 g) was used as a source of iron and left mixed with TEOS for 2 h. The resulting mixture then underwent microwave-assisted hydrothermal processing at 120 °C for a duration of 6 h. Following this step, the catalyst was desiccated at 110 °C overnight and later subjected to calcination at 550 °C for 6 h, culminating in the formation of the FSFe photocatalyst.

The deposition of metal oxides onto FSFe catalysts was achieved through an electrochemical technique, as outlined by the previous author [30]. The procedure commenced with the introduction of a TEAP (0.1 M) and distilled water (2 mL) solution into an electrochemical cell. The electrochemical cell consists of a Pt and a metal (Ag, Zr) plate as the cathode and anode electrode, respectively, with constant dimensions (2 cm × 2 cm). Electrolysis was carried out at a current density of 120 mA cm^{-1} under cold temperature (0 °C). Upon completion, the sample was dried overnight (110 °C) and subsequently subjected to calcination (550 °C) for 3 h. This methodology was equally applied in the synthesis of AgO/FSFe and ZrO_2/FSFe photocatalysts, employing Ag and Zr plates as respective sources. The AgO loading levels were varied at 3, 10, and 15 wt%, producing catalysts designated as 3AgO/FSFe, 10AgO/FSFe, and 15AgO/FSFe.

2.3 Characterization of Catalysts

The synthesized catalysts underwent rigorous and multifaceted characterization to elucidate their structural, morphological, and chemical characteristics. X-ray diffraction (XRD) was conducted using a Bruker Advance D8 diffractometer to investigate the crystal lattice and phase composition of each catalyst with precision. Nitrogen (N_2) physisorption techniques were employed to ascertain the total pore volume, average pore size, and BET (Brunauer–Emmett–Teller) surface area parameters essential to comprehending the surface topology of the catalysts. Morphological analysis was performed using Field Emission Scanning Electron Microscopy (FESEM) on a JEOL JSM-6701F microscope (Japan), allowing for high-resolution imaging of surface textures. Fourier transform infrared (FTIR) spectroscopy was applied using an Agilent Cary 640 spectrometer, aimed at identifying specific functional groups through the potassium bromide (KBr) method, spanning a wavenumber interval of 1400–400 cm^{-1} at room temperature. In this process, the catalyst and KBr were finely milled in a 0.001:0.1 proportion and compacted into pellets under pressures up to 10 MPa. Furthermore, UV–Vis Diffuse Reflectance Spectroscopy (UV–Vis DRS) was performed using a Perkin Elmer spectrophotometer (USA) within the 200–800 nm wavelength range to determine the material's optical band gap, utilizing the Kubelka–Munk (K–M) transformation for precise band gap analysis. To investigate the electronic and optical structure of the catalysts' photoluminescence (PL), a PTI QuantaMaster™ 60 Fluorescence Spectrophotometer, USA, was used. The sample was sandwiched between two glass slides and analyzed by the excitation of an Xe lamp (75 W) in the range of 200–1700 nm at room temperature. Electrochemical impedance spectroscopy (EIS) and Mott–Schottky analyses were conducted using a three-electrode system with the photocatalyst-coated FTO glass as the working electrode, Ag/AgCl as the reference electrode, and platinum wire as the counter electrode in a 0.5 M Na_2SO_4 electrolyte under dark and illuminated conditions. Lastly, X-ray Photoelectron Spectroscopy (XPS) was employed to delve into the electronic structure and oxidation states within the catalyst by measuring the kinetic energy of electrons emitted under X-ray exposure, providing valuable insight into the material's surface chemistry.

2.4 Simultaneous Photocatalytic Removal of Cr(VI) and MO

In this investigation, a batch reactor (Fig. S1) was employed, outfitted with a 400-nm metal halide lamp that generated visible light at a photon flux of 13.85 × 10^{-6} Em^{-2} s^{-1} and a power rating of 36 W. A recirculating cooling apparatus

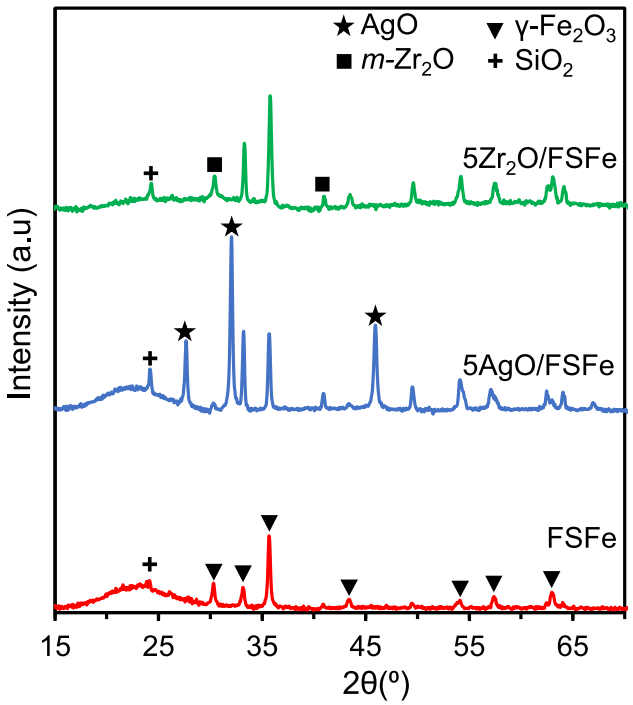

Fig. 1 XRD spectra of all synthesized catalysts

was incorporated to uphold a consistent thermal environment. A catalyst-laden mixture was prepared by combining it with a 50 mL solution containing Cr(VI) and MO, with pollutant concentrations ranging from 0.125 to 0.375 g/L (10–80 mg/L). The pH was meticulously calibrated between 1 and 7 using either HCl or NaOH to condition the solution for the pollutants. The suspension was stirred under dark conditions for one hour to establish adsorption–desorption equilibrium before commencing the photocatalytic process under light exposure. The reaction proceeded at a constant 25 °C for three hours, with samples collected at 30-min intervals and residual photocatalyst removed by centrifugation. Following each extraction, UV–Vis spectrophotometry (Cary 60 UV–Vis, Agilent Technologies, USA) was employed to monitor adsorption bands of MO (508 nm) and Cr(VI) (345 nm).

3 Results and Discussion

3.1 Characterization

3.1.1 Structures of Crystal and Phase

As shown in Fig. 1, the XRD spectra confirmed the crystal's nature and the phases' purity on all synthesized photocatalysts. A broad peak at the 17–28° range was spotted on all of the synthesized catalysts indicating the presence of amorphous SiO_2 (JCPDS file No. 29-0085). As previously reported for FSFe, the diffraction peaks of iron oxide inside FSFe were detected at 2θ = 30.3°, 33.2°, 35.6°, 43.5°, 53.0°, 57.4°, and 63.1° which corresponds to planes (220), (221), (311), (400), (422), (511), and (440), respectively, that exist in maghemite phase (γ-Fe_2O_3) (JCPDS file No. 39-1346) [26]. These iron oxide peaks were present in the XRD spectra of all $5ZrO_2$/FSFe and 5AgO/FSFe photocatalysts with a slight increment in their intensities indicating high crystallinity of all synthesized samples. Besides, additional peaks at 2θ of 30.41° (111), 24.30° (011), and 41.00° (211) occur inside $5ZrO_2$/FSFe indicating the presence of monoclinic ZrO_2 (JCPDS card No. 79-1771). Similarly to the 5AgO/FSFe photocatalyst, it shows additional peaks at 27.65° (110), 32.03° (111), and 45.95° (200) which indicates the presence of AgO (JCPDS file No. 43-1038) which is in line with the previous researcher who reported on the electrodeposition of silver nanoparticles [30, 43, 44]. The crystallite size for all synthesized catalysts was calculated using the Debye–Scherrer formula and is tabulated in Table 1.

3.1.2 Textural Study

Table 1 compiles the textural properties of all synthesized catalysts, offering valuable insight into their structural features relevant to catalytic performance. The incorporation of AgO and ZrO_2 onto FSFe resulted in a noticeable reduction in both the BET surface area and total pore volume, indicating partial pore blockage within the FSFe framework. This structural alteration is likely associated with the deposition of metal oxides inside the pores of FSFe [30, 31]. This structural modification is assumed to contribute positively to the photocatalytic performance, possibly through enhanced charge carrier separation, improved heterojunction formation, and facilitated generation of reactive radical species by the doped metal oxides. It may be inferred that among the metal oxide-loaded catalysts, 5AgO/FSFe exhibited the highest BET surface area (346 $m^2\ g^{-1}$) and total pore volume (0.69 $cm^3\ g^{-1}$) compared to $5ZrO_2$/FSFe. This observation is consistent with previous studies reporting that Ag doping reduces the surface area of α-Fe_2O_3 nanoparticles, which suggests that such structural modifications could influence the accessibility of active sites and, consequently, the overall catalytic behavior [45, 46].

The N_2 adsorption–desorption analysis (Fig. S2) reveals that all synthesized catalysts displayed an irreversible Type IV isotherm coupled with an H3 hysteresis loop (0.4–1.0 P/Po), a hallmark of mesoporous structures featuring slit-shaped pores, in accordance with IUPAC specifications [23]. A notable decrease in N_2 adsorption at elevated relative pressures was recorded following metal oxide incorporation, indicating successful metal oxide integration into

Table 1 Surface and textural properties of FSFe and metal oxide-modified FSFe catalysts

Catalyst	BET surface area[a] ($m^2\ g^{-1}$)	Total pore volume[b] ($cm^3\ g^{-1}$)	Crystallite size[c] (nm)
FSFe	493	0.90	6.93
5AgO/FSFe	346	0.69	6.99
$5ZrO_2$/FSFe	315	0.58	5.58

[a]Calculated from N_2 adsorption–desorption measurements using Brunauer–Emmett–Teller (BET) method at 537K
[b]Calculated from N_2 adsorption–desorption measurements using the non-local density functional theory (NLDFT) method
[c]Crystallite size calculated using the Debye–Scherrer formula

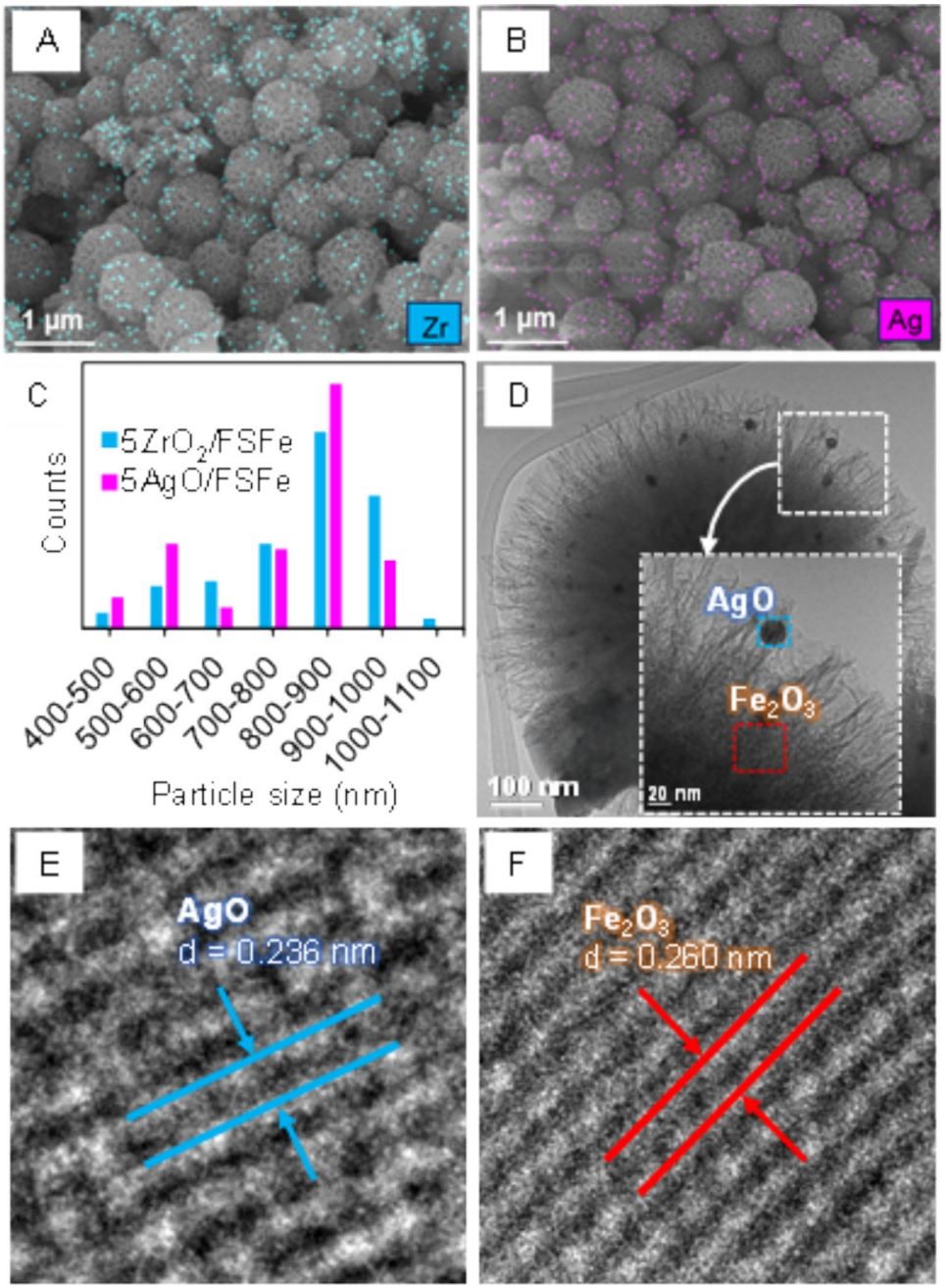

Fig. 2 FESEM mapping image of **A** $5ZrO_2$/FSFe and **B** 5AgO/FSFe. **C** Particle distribution of $5ZrO_2$/FSFe and 5AgO/FSFe. **D** TEM images of 5AgO/FSFe and **D** HR-TEM images for **E** AgO and **F** Fe_2O_3

the FSFe matrix, consequently inducing partial pore obstruction [31, 45]. Pore size distribution, assessed via nonlocal density functional theory (NL-DFT), corroborated the mesoporous configuration, in alignment with XRD findings. Each catalyst exhibited a multimodal pore size distribution with a distinct peak between 3 and 10 nm, attributed to the mesoporous framework created through the self-assembly of the CTAB surfactant during fibrous material synthesis [47].

3.1.3 Morphological Studies

Figure 2A, B presents the FESEM mapping image of the synthesized $5ZrO_2$/FSFe and 5AgO/FSFe catalysts. Each catalyst exhibits a bicontinuous concentric lamellar morphology, confirming that the distinctive FSFe structure remained intact following metal oxide incorporation [23, 48]. To delve deeper into the compositional intricacies and spatial distribution of metal oxides within the fibrous silica matrix, energy-dispersive X-ray (EDX) mapping was employed. The blue and purple markers signify the presence of Zr and Ag atoms, respectively. The mapping reveals a uniform dispersion of metal atoms throughout the fibrous silica iron framework. The particle size distributions (Fig. 2C) were derived from analyzing the areas of 100 individual particles across the synthesized catalysts, based on the FESEM imagery. From the data obtained, the average particle sizes for $5ZrO_2$/FSFe and 5AgO/FSFe were determined to be 805 and 768 nm, respectively. Although 5AgO/FSFe shows a smaller average particle size compared to $5ZrO_2$/FSFe, there is no significant effect on the particle size after doping metal oxides onto FSFe. However, further investigations were carried out to understand the positions of metal oxide particles inside FSFe using a 5AgO/FSFe catalyst in Transmission Electron Microscopy (TEM) images presented in Fig. 2D. The morphology of FSFe was not significantly altered by the addition of AgO (dark spot), indicating that the AgO incorporation process was successful. High-Resolution Transmission Electron Microscopy (HR-TEM) measurements of the interplanar distances of the Fe_2O_3 and AgO elements are 0.26 nm and 0.23 nm, respectively. These findings further supported the presence of these elements on 5AgO/FSFe (Fig. 2D, E) with the highest peak in XRD spectra for 5AgO/FSFe which indicates the plane of (311) and (200) for Fe_2O_3 and AgO, respectively.

3.1.4 Vibrational Spectroscopy

Figure 3 provides the infrared spectra for the dendritic fibrous FSFe-supported metal oxides derived from different metal oxides, highlighting the interaction of key functional groups. In Fig. 3A, dominant peaks appear within the 1400–400 cm^{-1} range, indicative of various functional groups present across

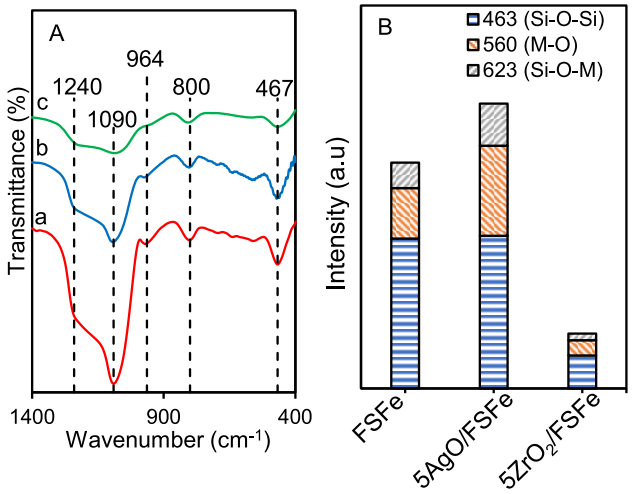

Fig. 3 **A** FTIR spectra of **a** FSFe **b** 5AgO/FSFe and **c** $5ZrO_2$/FSFe in the range of 400–1400 cm^{-1} and Gaussian peak area of the FTIR deconvolution peak at **B** 700–400 cm^{-1}

all catalysts. Notable peaks reveal the presence of an asymmetric Si–O–Si network (1240 and 1090 cm^{-1}), a Si–OH stretching band (964 cm^{-1}), Si–O–Si symmetric vibration (800 cm^{-1}), and Si–O–Si bending vibration (467 cm^{-1}) [30, 31]. These consistent bands across the catalysts confirm that the FSFe structure remains stable even after metal oxide incorporation, aligning with findings from XRD analyses.

Figure S3 presents the Gaussian curve-fitting analyses in the 700–400 cm^{-1} region, offering deeper insights into the metal–oxygen vibrational modes and their interactions with the fibrous silica iron framework. These spectral features further reflect the structural modifications induced by metal oxide incorporation within the synthesized catalysts. The transmittance intensities corresponding to each peak are summarized in Fig. 3B. The spectral region between 700 and 400 cm^{-1} was deconvoluted into three distinct peaks assigned to Si–O–Si (463 cm^{-1}), M–O (560 cm^{-1}), and Si–O–M (M = Ag, Zr) at 623 cm^{-1} [30, 31, 49]. This observation may suggest that AgO was more effectively incorporated into the FSFe framework through the desilication process, potentially forming stronger Si–O–Ag linkages. Such interactions could plausibly stabilize Ag within the silica iron matrix and may facilitate improved charge-transfer pathways, thereby enhancing the catalytic functionality. The wide range scan revealed a minor peak at 964 cm^{-1}, attributed to the stretching vibrations of silanol (Si–O–H) groups, with FSFe exhibiting the highest intensity [49]. Upon incorporation of metal oxides, the Si–O–H band intensity decreased, which could indicate the dehydrogenation of surface silanol groups through interactions with metal atoms during the electrolysis process, hence producing Si–O–M bonds. The desilication of Si–O–Si and the substitution of hydrogen atoms consequently result in the intensities

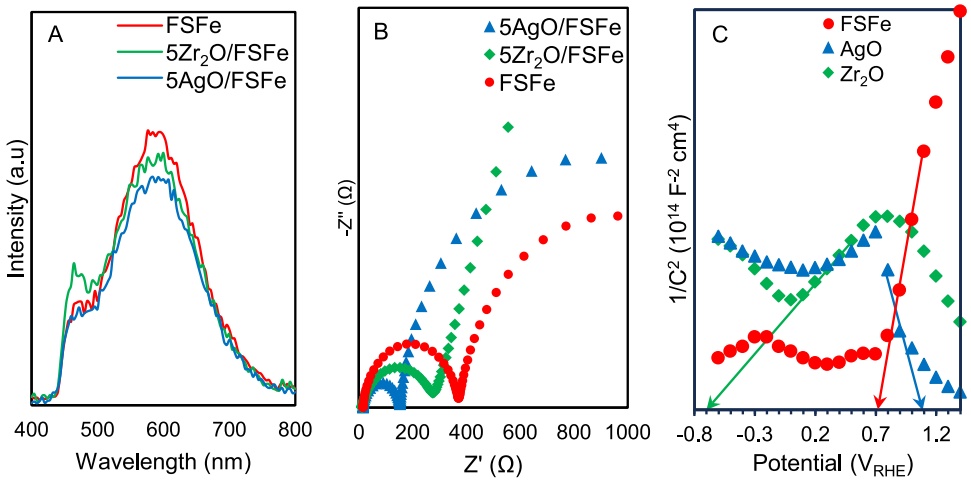

Fig. 4 **A** Photoluminescence spectra and **B** EIS Nyquist plots of the catalysts. **C** Mott–Schottky analysis for synthesized catalysts

of Si–O–M in 5AgO/FSFe, higher than $5ZrO_2$/FSFe catalysts. The augmentation of this band is anticipated to create a defect level between the activation energies of FSFe and AgO, which may effectively reduce the photocatalyst's band gap and thereby enhance its efficiency in the photocatalytic removal of Cr(VI) and MO.

3.1.5 Optical and Photoluminescence Properties and Chemical Oxidation State

The optical properties of the catalysts in their composite structures were analyzed through UV–Visible Diffuse Reflectance Spectra (UV–Vis/DRS) studies, employing the Kubelka–Munk equation (Eq. 1) for detailed assessment. The results of these analyses are illustrated in Fig. S4.

$$(\alpha h\upsilon)^2 = A\left(h\upsilon - E_g\right) \tag{1}$$

Key parameters analyzed include band gap energy (E_g), light frequency (υ), absorbance (A) (cm^{-1}), and Planck's constant (h). As shown in the inset of Fig. S4, the pristine band gaps of AgO and ZrO_2 were determined to be 1.75 and 3.10 eV, respectively, while the composite band gaps of 5AgO/FSFe and $5ZrO_2$/FSFe were measured at 1.80 and 1.95 eV following metal oxide incorporation. These results suggest that the electrodeposition of AgO narrowed the pristine FSFe band gap from 1.85 eV, thereby enhancing its responsiveness to visible light and facilitating the generation of reactive species that promote superior photocatalytic activity. In contrast, $5ZrO_2$/FSFe exhibited an opposite trend upon ZrO_2 deposition. This behavior is consistent with the quantum confinement effect, wherein the band gap energy inversely correlates with the crystallite size (below 10 nm) of the metal oxide-doped FSFe catalysts [50]. Supporting evidence from FTIR analysis further indicates that 5AgO/FSFe possesses the highest concentration of Si–O–M bonds within its catalyst matrix, reinforcing the enhanced structural integration of AgO.

Photoluminescence (PL) analysis is commonly used to evaluate the recombination of electron–hole pairs in photocatalysts, indicating the efficiency of charge carrier separation and mobility. PL spectra (400–800 nm) as presented in Fig. 4A revealed that the 5AgO/FSFe catalyst had much lower emission intensity than $5ZrO_2$/FSFe, suggesting fewer electron–hole recombination events. This decrease is attributed to AgO promoting heterojunction formation, which enhances charge transfer and reduces recombination [51]. Notably, 5AgO/FSZr exhibited the lowest PL intensity, indicating superior charge separation and movement. These findings are consistent with UV-DRS results, confirming the improved photocatalytic redox performance of the AgO/FSFe catalysts. Furthermore, this observation is further supported by the EIS analysis (Fig. 4B), where 5AgO/FSFe displays a markedly smaller arc diameter compared to $5ZrO_2$/FSFe and pristine FSFe. The reduced arc diameter may suggest lower charge-transfer resistance, which could imply a prolonged electron lifetime before recombination.

Mott–Schottky analysis was conducted to evaluate the flat-band potentials of the catalysts and to elucidate their semiconductor type and charge-transfer behavior, as illustrated in Fig. 4C. The plots revealed that FSFe and ZrO_2 exhibited negative slopes with flat-band intercepts at 0.73 and − 0.70 eV, respectively, indicative of *n*-type semiconducting behavior. In contrast, AgO displayed a positive slope, characteristic of a *p*-type semiconductor, with a corresponding flat-band potential of 1.10 eV. Together with the EIS and PL results, the Mott–Schottky analysis suggests that the *p–n* semiconductor alignment of AgO/FSFe promotes effective charge separation, which may account for the improved photocatalytic activity [32, 52].

The oxidation states of the FSFe and 5AgO/FSFe catalysts were ascertained by XPS inspection, as seen in Fig. 5.

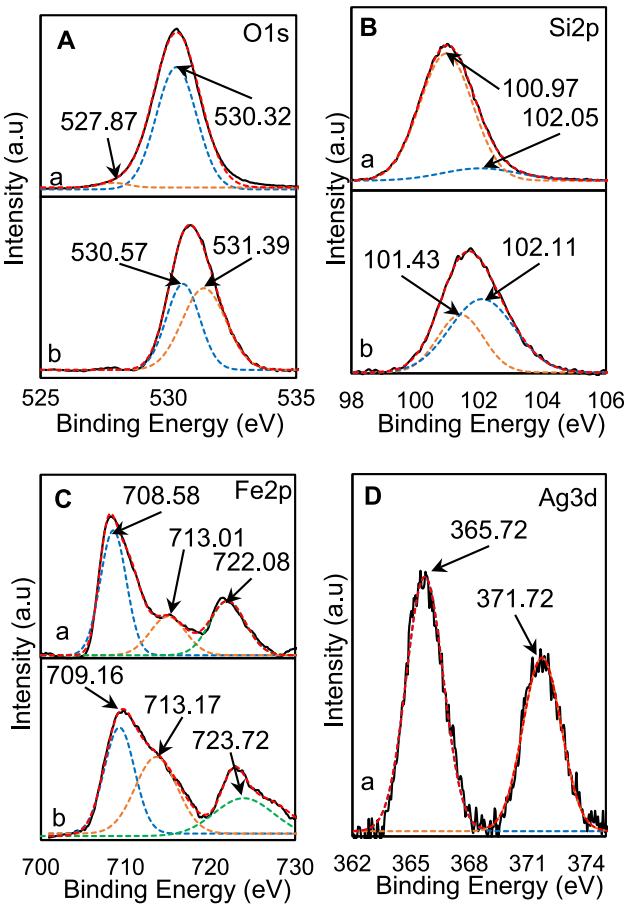

Fig. 5 XPS spectra of survey **A** O1*s*, **B** Si2*p*, and **C** Fe2*p* of **a** 5AgO/FSFe and **b** FSFe and **D** Ag3*d* of 5AgO/FSFe catalyst

Two distinct peaks were identified upon deconvolution of the O1*s* spectra of 5AgO/FSFe and FSFe. The O1s spectrum of FSFe (Fig. 5A/b) shows the peaks at 530.57 eV and 531.39 eV representing lattice oxygen (Si–O and/or Fe/O) and hydroxyl oxygen (–OH), respectively [26, 53]. After the addition of AgO (Fig. 5A/a), a red-shift phenomenon occurred where the binding energies shifted to the lower binding energy. This allows electron transfer from AgO to FSFe prompting a contact to form between the Si–O in FSFe and the AgO, resulting in the formation of the Si–O–Ag bond. Furthermore, the high intensities of the hydroxyl oxygen (530.32 eV) in 5AgO/FSFe would signify that more oxygen vacancies are present consequently increasing the carrier transfer rate [54]. The Si 2*p* spectrum is illustrated in Fig. 5B/b, where the deconvoluted peaks are at 101.43 eV (Si–O–Si) and 102.11 eV (Si–O–Fe). A significant decline in the Si–O–Fe peak was in line with findings from the FTIR analysis showing the possible substitution of Si or Fe atoms with Ag atoms. Figure 5C/b shows Fe2$p_{3/2}$ and Fe2$p_{1/2}$ peaks exist in FSFe, which correspond to 709.16 eV and 723.72 eV. Another satellite peak was observed at 713.17 eV in between Fe2$p_{3/2}$ and Fe2$p_{1/2}$ peaks assigned to the Fe^{3+} state in Fe_2O_3 of FSFe [26, 54]. The difference in binding energy between Fe2$p_{3/2}$ and Fe2$p_{1/2}$ peaks remains constant, indicating no formation of Fe^{2+} ions [55]. In Fig. 5D, AgO was discovered to have a doublet peak at 365.72 eV and 371.72 eV, with spin–orbit energy separations of 6 Ev [56].

3.2 Simultaneous Photocatalytic Removal of Cr(VI) and MO

Figure 6A, B illustrates the concurrent photocatalytic elimination of Cr(VI) and MO for the synthesized photocatalysts (5ZrO_2/FSFe, 5AgO/FSFe, and FSFe). To assess photocatalytic efficiency, the mixture of Cr(VI) and MO solutions was combined with each photocatalyst and stirred in darkness for an hour to reach adsorption–desorption equilibrium. Subsequently, visible-light exposure at a stable ambient temperature continued for three hours.

To examine the comparative performance of these metal oxide-modified catalysts, their simultaneous Cr(VI) reduction and MO degradation were evaluated. Upon 180 min of illumination, the FSFe photocatalyst exhibited the lowest efficiency in removing Cr(VI) (8.75%) and MO (24.10%), likely due to the rapid electron–hole recombination rate intrinsic to FSFe. The 5AgO/FSFe catalyst demonstrated superior efficacy, achieving Cr(VI) removal of 41.05% and MO degradation of 98.93%, outperforming 5ZrO_2/FSFe with photoremoval of 20.70% and 42.55%, respectively. The photocatalytic efficiency was markedly enhanced upon the integration of metal oxides with FSFe, suggesting the formation of a heterojunction between FSFe and the metal oxides.

The distinct behaviors in Cr(VI) photoreduction and MO photodegradation are elucidated in schematic band energy diagrams for AgO/FSFe and ZrO_2/FSFe as presented in Fig. 7. It is well known that in *n*-type semiconductors, the conduction band energy (E_{CB}) lies around 0.1–0.3 eV above the flat-band potential, while in *p*-type semiconductors the valance band energy (E_{VB}) lies around 0.1–0.3 eV below it [52, 57]. Therefore, with the flat-band potential obtained from Fig. 4C, the E_{CB} of FSFe and ZrO_2 was 0.43 and − 1.00 eV, respectively, whereas the E_{VB} of AgO was 1.40 eV. The band gap energy (E_G) of each composite, previously determined from Fig. S4, allows for calculation of the remaining E_{CB} and E_{VB} energies using Eq. 2 for each synthesized catalyst.

$$E_{VB} = E_{CB} + E_G \tag{2}$$

The estimated E_{CB} values for AgO are − 0.35 eV, while the calculated E_{VB} values for FSFe and ZrO_2 were 2.23 and 2.10 eV, respectively. For comparison, the position of E_{CB} and E_{VB} of pristine Fe_2O_3 was in the region of 0.31 and 2.15 eV, respectively [58]. Upon incorporation of

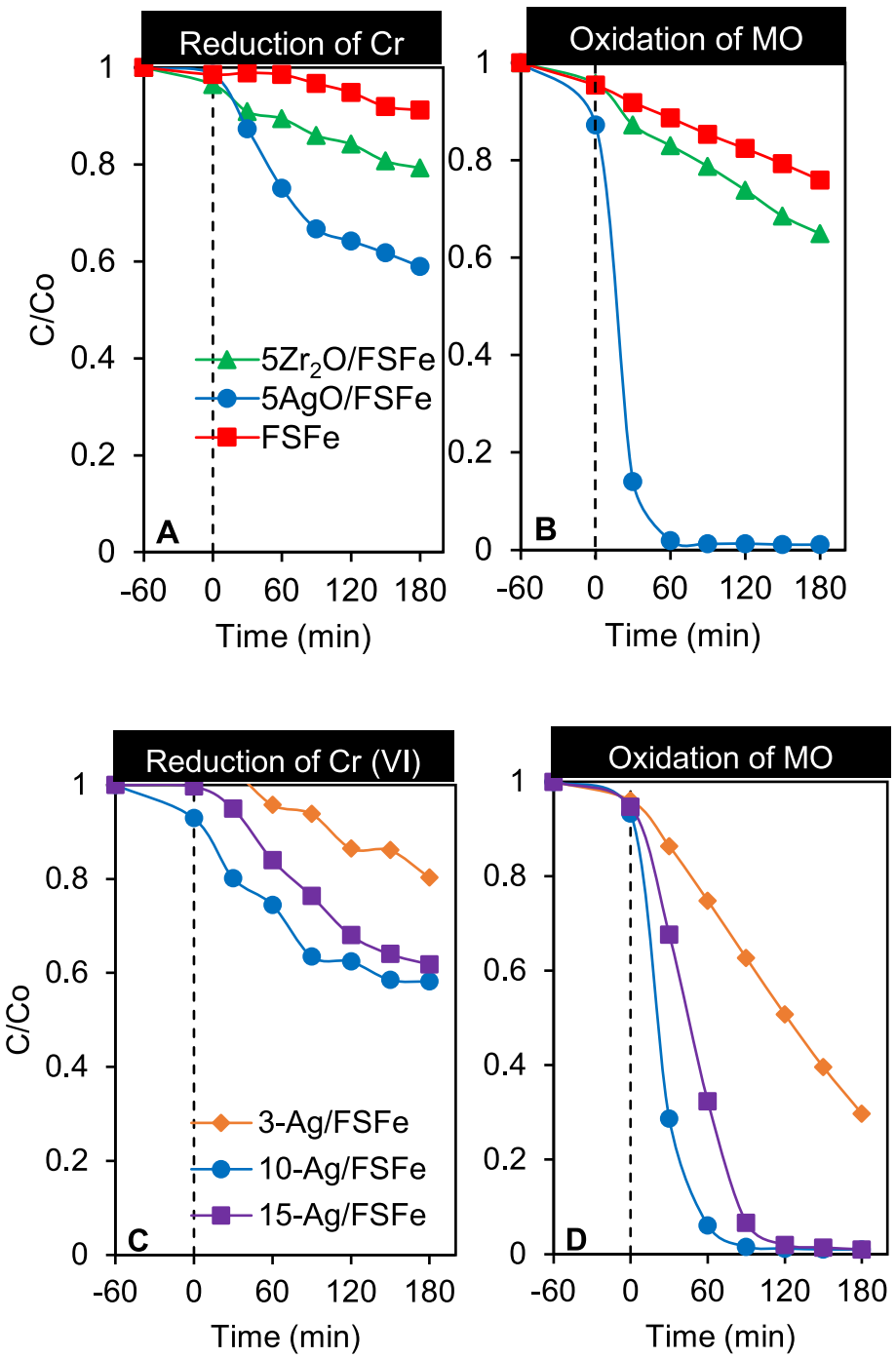

Fig. 6 **A** and **B** are the effect of different metal oxide doping onto FSFe photocatalyst, while **C** and **D** are the effect of different AgO loadings onto FSFe photocatalyst for simultaneous removal Cr(VI) and MO, respectively, [pH = 1, catalyst dosage = 0.125 g L^{-1}, [Cr(VI)] = 40 mg L^{-1} and [MO] = 10 mg L^{-1}]

Fe_2O_3 into the silica framework, the band positions of FSFe shifted toward the oxidative region for both E_{CB} and E_{VB}. Although the E_{VB} of FSFe is positioned close to the oxidation potential of H_2O, its E_{CB} remains more positive than the redox potential of Cr(VI)/Cr(III). This unfavorable alignment increases the probability of electron–hole recombination, as confirmed by the PL analysis. Hence, subsequent modification of FSFe with metal oxides (AgO and ZrO_2) effectively adjusts the E_{CB} position, thereby enhancing charge separation and improving the simultaneous photocatalytic removal of Cr(VI) and MO.

Furthermore, the schematic diagram illustrates that both systems are indicative of a Type II heterojunction, in which photogenerated electrons migrate from the conduction band of metal oxide (AgO, ZrO_2) to that of FSFe, while the corresponding holes transfer from the valence band of FSFe to

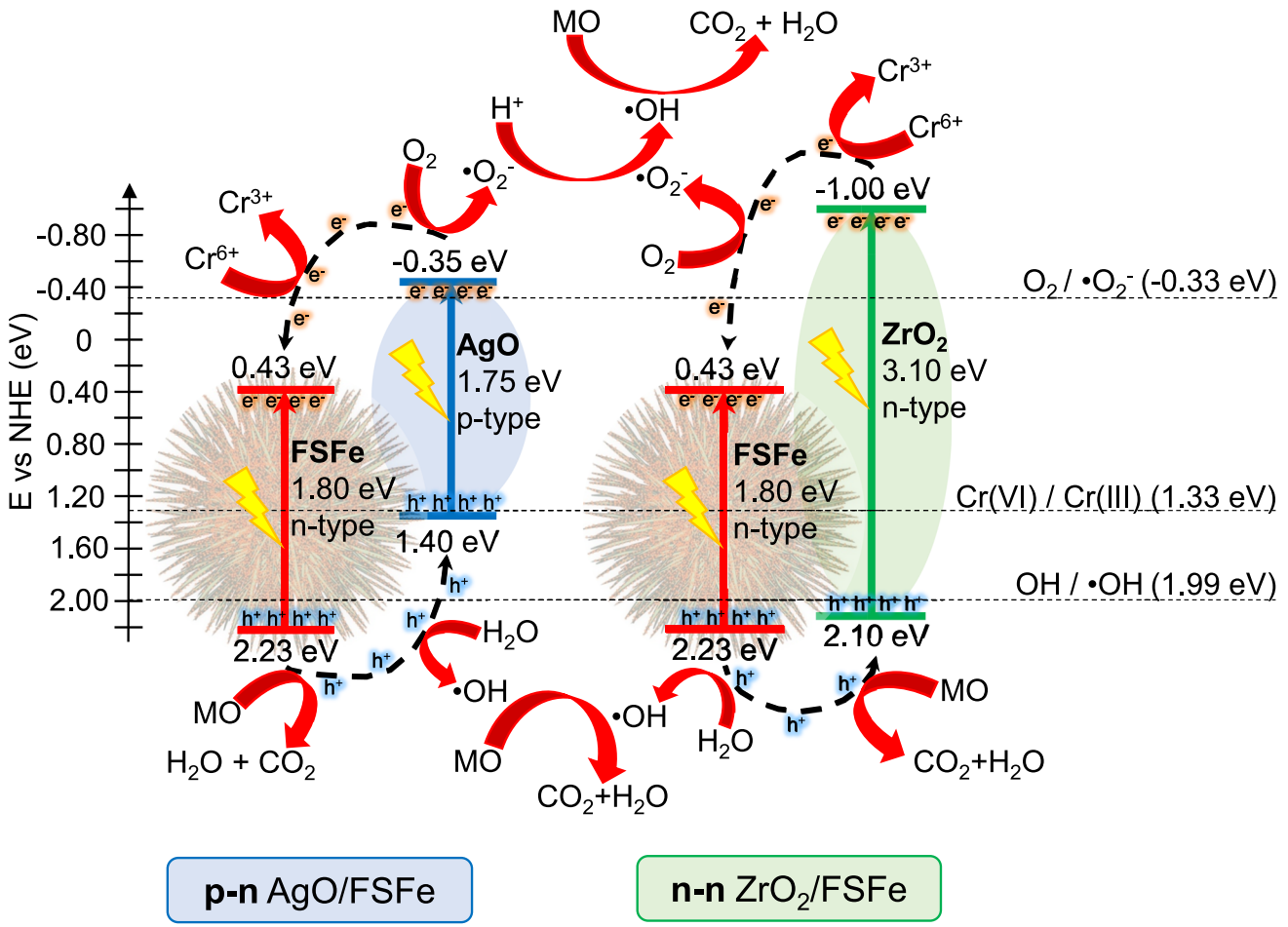

Fig. 7 Proposed mechanism for AgO/FSFe and ZrO_2/FSFe in simultaneous photocatalytic removal of Cr(VI) and MO

that of metal oxide. This staggered band alignment facilitates efficient spatial separation of charge carriers at the interface. The formation of a Type I heterojunction can be excluded, as the energy offset between the conduction band of FSFe and the valence band of the metal oxides is relatively large, thereby limiting the likelihood of direct electron–hole recombination [59]. Furthermore, a key distinction lies in the interfacial interactions, where the integration of AgO with FSFe gives rise to a *p–n* heterojunction, while the incorporation of ZrO_2 with FSFe results in an *n–n* junction. The formation of a *p–n* heterojunction is generally more favorable for facilitating efficient charge separation and suppressing electron–hole recombination, thereby enhancing photocatalytic activity, whereas *n–n* junctions typically exhibit less effective charge transfer across the interface [36, 37]. The FSFe catalyst exhibited the lowest efficiency in the photoremoval of Cr(VI) and MO, likely due to its limited capability for effective charge carrier separation, which accelerates electron–hole recombination and consequently diminishes its photocatalytic performance compared to the metal oxide-modified catalysts.

After the incorporation of metal oxides onto the FSFe catalyst, the photocatalytic removal efficiencies of Cr(VI) and MO were markedly enhanced. Both synthesized catalysts exhibited band edge positions that surpass the standard oxidation potential of $OH^-/\cdot OH$ ($E_\theta = +1.99$ eV vs NHE), the reduction potential of Cr(VI)/Cr(III) ($E_\theta = +1.33$ eV vs NHE), and the redox potential of oxygen $O_2/\cdot O_2^-$ ($E_\theta = -0.33$ eV vs NHE) [41, 60, 61]. These favorable band alignments suggest that the photogenerated electron–hole pairs can be effectively separated and exploited to drive the simultaneous reduction of Cr(VI) and degradation of MO. Compared with 5AgO/FSFe, the 5ZrO_2/FSFe catalyst exhibited noticeably poorer photocatalytic performance, which may be attributed to its unfavorably aligned band positions located further from the relevant redox potentials. This misalignment likely restricts the generation of reactive species such as ·OH radicals available to photocatalytically remove Cr(VI) and MO efficiently consequently promoting rapid electron–hole recombination. Moreover, 5AgO/FSFe demonstrates superior outcomes in the simultaneous photocatalytic removal of Cr(VI) and MO, not only due to its

narrow band gap, which enhances photon absorption, but also due to its advantageous band alignment that favors toward oxidation region, facilitating efficient transfer of photogenerated electrons and holes, thereby enhancing treatment efficacy for both heavy metal ions and organic dyes [62, 63].

Next, the effect of AgO loading was further studied as shown in Fig. 6C, D. AgO/FSFe was synthesized with three different weight loadings of AgO, which are 3, 10, and 15 wt%. From the figure, it can be observed that the simultaneous photocatalytic removal of Cr(VI) and MO for 10AgO/FSFe was the highest performance up to 41.84% and 99%, respectively. It is recorded low in photocatalytic redox removal of pollutants at 3wt% was attributed to a higher rate of charge carriers recombination, whereas at 15wt% of AgO, the occurrence of the shading effect could hinder the exposure of active sites to visible light [30, 64]. Therefore, 10AgO/FSFe has been used for further studies in photocatalytic performance.

The pH of the pollutant solution plays a pivotal role in determining the chemical composition of the contaminants, the surface charge of the photocatalyst, and the affinity of the pollutant to adsorb onto the catalyst's surface. As depicted in Fig. S5, the simultaneous photocatalytic elimination of Cr(VI) and MO by 5AgO/FSFe is markedly influenced by the pollutant pH, with removal efficiency amplifying as the pH decreases. Optimal photocatalytic reduction of Cr(VI) and MO degradation was observed at extreme acidic condition (pH 1), achieving removal efficiencies of 41.84% and 99%, respectively. According to Le Chatelier's principle, H^+ ions facilitate the reduction of Cr(VI) to Cr(III), promoting a favorable reaction pathway in acidic environments (Eqs. 3, 4). Conversely, in alkaline conditions, the presence of OH^- ions adversely impacts the process, as they reduce the solution's acidity, effectively hindering the reaction's progress (Eq. 5) [65].

$$HCrO_4^- + 7H^+ + 3e^- \rightarrow Cr^{3+} + 4H_2O \quad (3)$$

$$Cr_2O_7^{2-} + 14H^+ + 6e^- \rightarrow 2Cr^{3+} + 7H_2O \quad (4)$$

$$CrO_4^{2-} + 4H_2O + 3e^- \rightarrow Cr(OH)_3 + 5OH^- \quad (5)$$

When the pH_{pzc} of the catalyst commonly at pH6 was higher than the system's pH, the catalyst surface gains a positive charge, leading to more protonated sites. Research has shown that this positively charged surface can enhance electrostatic attraction with primary chromium species, especially in acidic environments containing ions like $Cr_2O_7^{2-}$ and $HCrO_4^-$, aiding in the reduction of Cr(VI) [30, 65]. Under acidic conditions, the molecular structure of methyl orange (MO) shifts into a quinone form, which is more readily oxidized than its azo form, typically seen in basic media [66, 67]. A pH of 1, with its high H^+ ion concentration, creates ideal conditions for this quinone form to be drawn to catalyst sites, increasing the catalyst's ability to produce hydroxyl radicals and enhancing photocatalytic activity [68, 69]. As pH rises, the reaction efficiency drops due to an increase in competing hydroxyl groups, which interfere with azo dye oxidation. Supporting evidence for MO's quinone structure at low pH includes shifts in both absorbance peak and color. Although the optimal photocatalytic performance of Cr(VI) and MO on 10AgO/FSFe occurs at pH 1, pH 3 was chosen for further studies to adhere to environmentally ethical practices.

To examine the effect of catalyst dosage on the concurrent photocatalytic removal of Cr(VI) and MO, the catalyst amount of 10AgO/FSFe varied from 0.125 to 0.375 g L^{-1}. Initial pollutant concentrations were set at 40 mg L^{-1} for Cr(VI) and 10 mg L^{-1} for MO, with a pH level of 3. As shown in Fig. S6, the optimal catalyst dosage was determined to be 0.25 g L^{-1}, yielding maximal photocatalytic removal efficiencies of 99.35% for MO and 49.80% for Cr(VI). A further increase in dosage to 0.375 g L^{-1} resulted in a shielding effect, limiting light penetration and subsequently diminishing removal efficacy [70].

The study also evaluated the influence of initial pollutant concentration ratios, ranging from 10 to 80 mg L^{-1} for Cr(VI) with MO held constant at 10 mg L^{-1}, to assess the kinetics of simultaneous photocatalytic removal using 10AgO/FSFe. The investigation considered the impact of initial pollutant concentration on the removal performance of both the target pollutant and the adjacent contaminant within the system. To model the impact of initial concentrations on the catalyst's efficacy, the Langmuir–Hinshelwood kinetic model (Eq. 6) was applied, allowing for an analysis of the optimal 10AgO/FSFe catalyst's kinetic parameters in the photocatalytic process. This model was derived through Eq. 7 for comprehensive kinetic evaluation.

$$\ln C_t = -kt + \ln C_o \quad (6)$$

$$\ln(C_o/C_t) = kt \quad (7)$$

Here, C_t and C_o represent the concentrations of the model pollutant at a specific time (t) and at the initial time ($t = 0$), respectively, with k denoting the pseudo-first-order rate constant. The simultaneous photocatalytic removal of Cr(VI) and MO using the 10AgO/FSFe catalyst follows a pseudo-first-order kinetic model, as indicated by the linear correlation between $\ln(C_o/C_t)$ and irradiation time (Fig. S7A-B). Table S1 summarizes the apparent rate constant (k_{app}) and the initial rate (r_o) for Cr(VI) and MO, with the coexisting pollutant concentration maintained at 10 mg L^{-1}.

The peak k_{app} value for Cr(VI) reduction was observed at an initial concentration of 20 mg L^{-1}, achieving 5.40 × 10^3 min^{-1} when the initial concentration of MO was constant at 10 mg L^{-1}, and the initial Cr(VI) concentration was varied between 10 and 80 mg L^{-1}. Beyond this concentration, Cr(VI) photoreduction decreased as competitive adsorption between pollutants for active sites and limited active species separation [71]. When the initial MO concentration was varied from 10 to 80 mg L^{-1} while keeping Cr(VI) constant, the maximum k_{app} (21.90 × 10^3 min^{-1}) was recorded when the MO concentration was at 10 mg L^{-1}. The observed reduction in reaction rate with increased MO concentration was attributed to limited photon penetration into the catalyst due to a shortened optical path length at higher MO levels [72]. Moreover, Eq. 8 served as a reference in constructing the Langmuir–Hinshelwood kinetic model.

$$\left(1/k_{app}\right) = (1/k_r K_{LH}) + (C_o/k_r) \tag{8}$$

Here, k_r indicates maximum reaction rate achievable under ideal conditions ($mgL^{-1}min^{-1}$), K_{LH} is the Langmuir–Hinshelwood adsorption constant, reflecting the affinity of the pollutant for the catalyst surface (L mg^{-1}), and C_o represents the initial pollutant concentration (mg L^{-1}). As stated in Table S1, it can be observed that the k_r and K_{LH} values for reduction of Cr(VI) were 0.944 mg L^{-1} min^{-1} and 0.003 L $mg^{-1,}$ respectively, proving that the adsorption of Cr(VI) onto the catalyst surface is the primary rate-limiting step. Conversely, for MO degradation, the values of k_r and K_{LH} were 0.05 mg L^{-1} min^{-1} and 0.12 L mg^{-1}, suggesting that the reaction's rate-limiting step predominantly occurs in the bulk solution rather than on the catalyst surface. These divergent values elucidate the underlying mechanisms at each phase of the reaction, providing valuable insight into the distinct kinetic processes governing the removal of each pollutant.

Figure S8A-B is employed to elucidate the influence of one pollutant's initial concentration on the adjacent pollutant within a simultaneous pollutant system. In particular, Fig. S8A illustrates that the photoreduction of Cr(VI) reaches its peak efficiency when the initial concentration of MO is maintained at 10 mg L^{-1}. However, a marked decrease in Cr(VI) reduction efficiency is observed as the concentration of MO escalates. Elevated concentrations of this acidic dye inhibit Cr(VI) from adequately binding to the active sites of the catalyst, thereby diminishing the conversion of Cr(VI) to its less toxic form [73]. Contrastingly, as depicted in Fig. S8B, variations in the initial concentration of Cr(VI) exert minimal influence on the photodegradation efficacy of MO. Consequently, an initial concentration ratio of 20 Cr(VI):10 MO is deemed optimal, and this ratio will be maintained as a constant parameter in subsequent experiments.

To further evaluate the photocatalytic efficiency of 10AgO/FSFe in the dual removal of Cr(VI) and MO, additional experiments were conducted under visible-light irradiation under varying conditions, as illustrated in Fig. S9A-B. In the absence of a catalyst (photolysis system), the removal efficiencies of Cr(VI) (9%) and MO (12.5%) were negligible, confirming that the incorporation of 10AgO/FSFe substantially enhances both the photoreduction of Cr(VI) and the photodegradation of MO. Moreover, the results indicate that the removal efficiencies of Cr(VI) and MO were significantly higher in the simultaneous pollutant system compared with the single-pollutant systems (19.16% and 38.21%, respectively). This enhanced performance can be attributed to the more effective separation of photogenerated electron–hole pairs. Overall, the findings suggest that in this work, the dual photocatalytic system predominates, as both pollutants concurrently exploit the oxidative and reductive reactive species for their removal.

3.3 Mechanism

In Fig. S10A-B, scavenger tests were conducted on 10AgO/FSFe toward photoreduction of Cr(VI) and photodegradation of MO, respectively, to identify the effect of different reactive species on the photocatalytic performance. Scavenging agents such as potassium carbonate (K_2CO_3), potassium chlorate ($KClO_3$), and sodium hydrogen carbonate ($NaHCO^3$) were used to trap reactive species e^-, h^+ and ·OH present inside the system, respectively [30]. From Fig. S10A, after the addition of K_2CO_3, the photoreduction of Cr(VI) drops tremendously from 64.37% to 22.23%, while photodegradation of MO remains constant [74]. Similarly, when $KClO_3$ was added into the system, the photoreduction of Cr(VI) remains unchanged, whereas the photodegradation of MO reduces slightly from 99.45% to 98.85%. The unaffected result in the performance of photoremoval of Cr(VI) and MO implies that the respective active species does not contribute to or inhibit the photocatalytic reactions between the catalyst and the pollutants. On the other hand, when $NaHCO^3$ was distributed homogenously into the photocatalytic system, the reduction of Cr(VI) decreased slightly from 64.37% to 60.87%, indicating that there is a possible reduction of Cr(VI) by ·OH. However, it can also be seen that there was a significant decline from 99.45% to 97.94% for the photodegradation of MO. Hence, it can be concluded that e^- was the predominant active species that contributed to the photoreduction of Cr(VI), whereas ·OH played a significant role in the photodegradation of MO. The findings were also in line with the kinetic studies that prove the majority of Cr(VI) reduction occurs due to the abundance of e^- on the surface, while the majority of MO degrade due to loads of ·OH present in the bulk medium.

To explore in depth on synergistic mechanism of AgO/FSF in the visible-light irradiation, an energy band structure was proposed (Fig. 7). In accordance with the findings of E_{VB} and E_{CB} above, during the absence of visible light, the acidic medium allows the Cr(VI) and MO to exist in anionic form, which then attracts to the positively charged AgO/FSFe catalyst. When visible light is introduced into the system, the electrons in the valence band of FSFe and AgO are excited to create electron–hole pairs (Eq. 9). Consequently, under the Type II heterojunction pathway, the photogenerated electrons migrate from the conduction band of AgO to the conduction band of FSFe, leading to electron accumulation at the E_{CB} of FSFe, while the photogenerated holes transfer from the valence band of FSFe to the valence band of AgO, resulting in hole accumulation at the E_{VB} of AgO. This spatial charge separation effectively suppresses electron–hole recombination and promotes the generation of reactive species, thereby enhancing the overall photocatalytic performance. A similar charge-transfer pathway can be proposed for the ZrO_2/FSFe system; however, the formation of an *n–n* heterojunction, rather than a *p–n* interface, leads to inefficient charge separation and accelerated electron–hole recombination. This mechanistic limitation is corroborated by the larger Nyquist arc radius in EIS analysis and the stronger PL emission intensity of ZrO_2/FSFe, both of which reflect poorer charge carrier dynamics. Consequently, ZrO_2/FSFe exhibits inferior photocatalytic performance compared with the highly efficient *p–n* heterojunction established in AgO/FSFe.

According to the calculated band energies, $\cdot O_2^-$ was produced in both AgO/FSFe and ZrO_2/FSFe photocatalysts due to the E_{CB} value of AgO and ZrO_2 being higher compared to the standard redox potential of $O_2/\cdot O_2^-$ ($E_\theta = -0.33$ eV vs. NHE) (Eq. 10) [24]. The substantial improvement in MO photodegradation by AgO/FSFe compared with ZrO_2/FSFe can presumably be attributed to the favorable alignment of AgO's conduction band with the standard redox potential of $O_2/\cdot O_2^-$, which facilitates efficient redox processes. Conversely, the poor photocatalytic response of ZrO_2/FSFe is likely due to the unfavorable band alignment and the pronounced recombination of photogenerated charge carriers, both of which severely hinder its ability to degrade MO.

$$\text{AgO/FSFe} + h\nu \rightarrow e^- + h^+ \tag{9}$$

$$O_2 + e^- \rightarrow \cdot O_2^- \tag{10}$$

Simultaneously, the photo-induced holes (h^+) present in the E_{VB} of AgO and FSFe advance to the surface of the photocatalyst, instigating a direct oxidative degradation process of MO as delineated in Eq. 11. Furthermore, the E_{VB} potential of FSFe surpasses that of hydroxyl radicals, $H_2O/\cdot OH$ (1.99 eV), enabling the generation of ·OH radicals through h^+ to facilitate the oxidation of MO, as outlined in Eqs. (12–14). Consistent with prior predictions from scavenger analyses, these findings underscore that ·OH and h^+ are the predominant reactive entities causing the photodegradation of MO. The complete decomposition of MO can thus be attributed to the active intervention of these reactive species.

$$\text{MO} + h^+ \rightarrow \text{Degradation of MO} \tag{11}$$

$$OH^- + h^+ \rightarrow \cdot OH \tag{12}$$

$$\cdot OH + \text{MO} \rightarrow \text{Degradation of MO} \tag{13}$$

$$\text{Degradation of MO} \rightarrow CO_2 + H_2O \tag{14}$$

$$\text{Cr(VI)} + 3e^- \rightarrow \text{Cr(III)} \tag{15}$$

Similarly, Eq. (15), which describes the mechanisms underlying the reduction of Cr(VI) to Cr(III), is shown. The photogenerated electron produced on both catalysts can undergo the photoreduction of Cr(VI) to Cr(III), as the redox potential of Cr(VI)/Cr(III) ($E_\theta = +1.33$ eV vs NHE) is more positive than the E_{CB} on both AgO and FSFe. However, since the nature of photogenerated electrons is unstable at lower energy levels, these excited electrons tend to recombine with h^+ in the E_{VB}. The incorporation of AgO into FSFe would inhibit this unfavorable process from occurring due to efficient charge transfer between these two heterojunctions. From previous oxidation state studies, the transfer of charges from AgO to FSFe would support the inability of photogenerated electrons to remain on the E_{CB} of AgO and further transport to a higher possible energy level, which was the E_{CB} of the FSFe catalyst. In comparison with pristine FSFe, this modification would produce an abundance of electrons on the E_{CB} of FSFe and consequently enhance the photoreduction of Cr(VI) to Cr(III). The addition of AgO enhances charge transfer within the AgO/FSFe heterojunction, allowing for more effective charge consumption. In contrast with ZrO_2/FSFe, the misaligned E_{VB} of ZrO_2 in the ZrO_2/FSFe composite likely hampers the effective separation of photogenerated holes, thereby suppressing their participation in redox reactions and consequently limiting the reduction of Cr(VI) to Cr(III). Therefore, the 10AgO/FSFe setup promotes charge separation and migration, optimizing reactive species for effective photocatalytic removal of these pollutants.

3.4 Effect of Organic Dyes, Reusability, and Stability

Since the actual effluent of industrial wastewater contains other types of organic dye, a study on the behavior of the outperforming photocatalyst on different dyes is significant. The

simultaneous photocatalytic reduction of Cr(VI) and degradation of organic dyes by 10AgO/FSFe were investigated, where the organic dye component was varied separately among MO, Rhodamine B (RhB), Methylene Blue (MB), and Congo Red(CR) as shown in Fig. S11A, B. From the figure, it can be observed that the photoreduction of Cr(VI) was the highest when it was mixed with RhB (87.50%) followed by MO (64.37%), CR (27.40%), and MB (0.72%) after exposure to light for 180 min. The same trends were also observed in the performance photodegradation of organic dyes, which shows the highest for RhB (99.78%) followed by MO (99.45%), CR (87.37%), and MB (66.41%). The photoremoval of Cr(VI) and organic dye for RhB gave the highest performance, possibly due to its highly conjugated chromophores, which efficiently absorb visible light to generate reactive oxygen species (ROS), while its strong surface adsorption and electron-rich groups promote effective oxidative degradation [75, 76]. The photoremoval of Cr(VI) and organic dye for CR exhibits lower efficiency than MO, likely attributable to the simpler molecular structure and smaller size of the MO molecule. This facilitates easier access to active sites on the photocatalyst surface, resulting in more efficient degradation, despite both being classified as azo dyes [77–79]. Furthermore, the photoremoval efficiency of Cr(VI) and organic dye for MB is inferior when compared to that of RhB, MO, and CR. This discrepancy arises from the more effective degradation of MO, attributed to a stronger electrostatic attraction between its anionic form and the positively charged catalyst surface. In contrast, MB, being cationic, encounters repulsion, resulting in reduced adsorption despite the increased generation of ROS under acidic conditions [80].

The potential to recover and reuse a catalyst in photocatalysis is particularly promising for reducing operating costs, and it could support the broader adoption of photocatalysis as an effective method for wastewater treatment. In repeating experiments, 10AgO/FSFe was tested for its stability in reducing Cr(VI) and degrading MO, with results illustrating the catalyst's resilience. Even after three successive cycles, the catalyst continued to degrade MO, underscoring its strong photocatalytic performance and reusability (Fig. S12). Across five cycles, a marked reduction in Cr(VI) levels was observed, possibly due to re-oxidation of Cr(VI) to Cr(III), demonstrating the composite's effectiveness and endurance in practical applications [81].

Table S2 provides a summary of selected studies on photocatalytic removal of pollutants by previous researchers. 10AgO/FSFe showed the best photodegradation of MO compared to other photocatalysts probably due to well-formed heterojunction formation and unique morphology of the unique fibrous morphology. Li et al. reported high degradation of MO, whereas Kosyuren et al. presented excellent photoreduction of Cr(VI) [82, 83]. This unfavorable reaction however focused on a single system which caused the possible interaction between oxidation and reduction was not explored effectively. Huang-Mu et al. presented an innovative approach utilizing both reduction and oxidation in the photocatalytic removal of two organic pollutants which are reactive red 120 (RR 120) and orange II (O-II) [84]. Several researchers also had been focused on simultaneous photocatalytic reduction and degradation of heavy metal and organic pollutant, respectively [30, 85, 86]. Continuous development of new photocatalysts in simultaneous photocatalytic removal of Cr(VI) and MO has shown promising results; however, high catalyst dosage and longer reaction time could become costly to be upscale [26, 87, 88]. Fibrous silica iron (FSFe) was previously developed for removing pollutants via photo and photo-Fenton processes, but due to its limited Cr(VI) reduction, incomplete performance, and reliance on hydrogen peroxide, its enhancement is imperative for superior pollutant elimination [26]. 10AgO/FSFe demonstrates promising potential in developing more efficient photocatalytic materials for the simultaneous remediation of heavy metal and organic contaminants.

4 Conclusion

In conclusion, a novel fibrous silica iron (FSFe) photocatalyst doped with silver oxide (AgO) and zirconium dioxide (ZrO_2) was successfully developed through microemulsion–electrolysis synthesis. Structural analysis confirmed the uniform dispersion of AgO nanoparticles on the fibrous framework, with FTIR revealing the formation of Si–O–M bonds that indicate strong chemical interactions. XPS further validated electron transfer from AgO to FSFe, reinforcing the formation of an efficient *p–n* heterojunction. Among the catalysts, 10AgO/FSFe exhibited outstanding photocatalytic activity, achieving 64.37% Cr(VI) reduction and 99.45% MO degradation under optimized conditions (pH 3, 0.25 g L^{-1} catalyst dosage, and initial concentrations of 20 mg L^{-1} Cr(VI) and 10 mg L^{-1} MO). Scavenger experiments confirmed that photogenerated electrons predominantly drive Cr(VI) reduction, while ·OH radicals are the main contributors to MO degradation. Notably, the simultaneous removal system outperformed the single-pollutant system due to the efficient consumption of both oxidative and reductive species. Beyond MO, the catalyst also demonstrated high activity toward other dyes (RhB > MO > AB > CR > MB), confirming its broad applicability. Moreover, the 10AgO/FSFe catalyst retained excellent performance over five successive cycles, underscoring its durability and stability. Collectively, these findings demonstrate that integrating Fe_2O_3 into a fibrous silica framework, coupled with the incorporation of AgO onto FSFe, induces an oxidative band alignment shift and establishes a robust *p–n* heterojunction. This configuration

promotes superior charge separation, broad-spectrum pollutant degradation, and excellent reusability, positioning the material as a promising candidate for advanced wastewater treatment applications.

Supplementary Information The online version contains supplementary material available at https://doi.org/10.1007/s13369-025-11011-1.

Acknowledgements The authors extend their gratitude to the Universiti Teknologi Malaysia for the financial backing provided by the Matching Grant MG2-42.1 (grant number 04M69) and the UTM Fundamental Research (UTMFR) (grant number 24H34). Further acknowledgments go to Universiti Teknologi Malaysia for awarding the Zamalah Scholarship to Nur Izzati Hannani Hazril, as well as to the Kurita Water and Environment Foundation Research Grant Program 2023 (grant number 4J652). The authors gratefully acknowledge the Nippon Sheet Glass Foundation for Materials Science and Engineering Research Grant (No.1U091).

Author Contributions Nur Izzati Hannani Hazril helped in writing—original draft, visualization, resources, methodology, investigation, formal analysis. Aishah Abd Jalil contributed to conceptualization, writing—review and editing, supervision, project administration, funding acquisition, validation. Nurul Sahida Hassan contributed to writing—review & editing, visualization, validation, formal analysis. Liew Shi Yan, Muhammad Hakimi Sawal, Nik Muhammad Izzudin, Muhammad Hafizuddin Mohd Sofi, Nurfatehah Wahyuny Che Jusoh, Faiz Arith, Sudiyarmanto Sudiyarmanto helped in writing—review & editing.

Funding Open access funding provided by The Ministry of Higher Education Malaysia and Universiti Teknologi Malaysia.

Declarations

Competing interest The authors declare that they possess no identifiable financial conflicts of interest or personal affiliations that could have potentially impacted the integrity or impartiality of the research presented in this manuscript.

References

1. Ajiboye, T.O.; Oyewo, O.A.; Onwudiwe, D.C.: Simultaneous removal of organics and heavy metals from industrial wastewater: a review. Chemosphere (2021). https://doi.org/10.1016/j.chemosphere.2020.128379
2. Zhang, H.; Li, R.; Zhang, Z.: A versatile EDTA and chitosan bi-functionalized magnetic bamboo biochar for simultaneous removal of methyl orange and heavy metals from complex wastewater. Environ. Pollut. (2022). https://doi.org/10.1016/j.envpol.2021.118517
3. Behera, M.; Nayak, J.; Banerjee, S.; Chakrabortty, S.; Tripathy, S.K.: A review on the treatment of textile industry waste effluents towards the development of efficient mitigation strategy: an integrated system design approach. J. Environ. Chem. Eng. **9**, 105277 (2021). https://doi.org/10.1016/J.JECE.2021.105277
4. Kamar, M.T.; Elattar, H.; Mahmoud, A.S.; Peters, R.W.; Mostafa, M.K.: A critical review of state-of-the-art technologies for electroplating wastewater treatment. Int. J. Environ. Anal. Chem. (2024). https://doi.org/10.1080/03067319.2022.2098486
5. Chen, S.; Huang, Y.; Han, X.; Wu, Z.; Lai, C.; Wang, J.; Deng, Q.; Zeng, Z.; Deng, S.: Simultaneous and efficient removal of Cr(VI) and methyl orange on LDHs decorated porous carbons. Chem. Eng. J. **352**, 306–315 (2018). https://doi.org/10.1016/J.CEJ.2018.07.012
6. Farhan Hanafi, M.; Sapawe, N.: A review on the water problem associated with organic pollutants derived from phenol, methyl orange, and remazol brilliant blue dyes. Mater. Today Proc. **31**, A141–A150 (2020). https://doi.org/10.1016/J.MATPR.2021.01.258
7. Sharma, P.; Singh, S.P.; Parakh, S.K.; Tong, Y.W.: Health hazards of hexavalent chromium (Cr (VI)) and its microbial reduction. Bioengineered **13**(3), 4923–4938 (2022). https://doi.org/10.1080/21655979.2022.2037273
8. Tumolo, M.; Ancona, V.; De Paola, D.; Losacco, D.; Campanale, C.; Massarelli, C.; Uricchio, V.F.: Chromium pollution in European water, sources, health risk, and remediation strategies: an overview. Int. J. Environ. Res. Public Health **17**, 5438 (2020). https://doi.org/10.3390/IJERPH17155438
9. Tufail, M.A.; Iltaf, J.; Zaheer, T.; Tariq, L.; Amir, M.B.; Fatima, R.; Asbat, A.; Kabeer, T.; Fahad, M.; Naeem, H.; Shoukat, U.; Noor, H.; Awais, M.; Umar, W.; Ayyub, M.: Recent advances in bioremediation of heavy metals and persistent organic pollutants: a review. Sci. Total. Environ. **850**, 157961 (2022). https://doi.org/10.1016/J.SCITOTENV.2022.157961
10. Chen, W.; He, X.; Jiang, Z.; Li, B.; Li, X.; Lin, L.: A capacitive deionization and electro-oxidation hybrid system for simultaneous removal of heavy metals and organics from wastewater. Chem. Eng. J. **451**, 139071 (2023). https://doi.org/10.1016/J.CEJ.2022.139071
11. Cui, J.; Ye, L.; Chen, X.; Li, J.; Yang, B.; Yang, M.; Yang, Q.; Yun, D.; Sun, S.: Simultaneously promoting adsorption and charge separation in Z-scheme ZnO/Cu_2O heterojunctions for efficient removal of tetracycline. Appl. Surf. Sci. **638**, 158046 (2023). https://doi.org/10.1016/J.APSUSC.2023.158046
12. Tijani, J.O.; Fatoba, O.O.; Madzivire, G.; Petrik, L.F.: A review of combined advanced oxidation technologies for the removal of organic pollutants from water. Water Air Soil Pollut. (2014). https://doi.org/10.1007/s11270-014-2102-y
13. Basem, A.; Jasim, D.J.; Majdi, H.S.; Mohammed, R.M.; Ahmed, M.; Al-Rubaye, A.H.; kianfar, E.: Adsorption of heavy metals from wastewater by chitosan: a review. Results Eng. **23**, 102404 (2024). https://doi.org/10.1016/J.RINENG.2024.102404
14. Ezugbe, E.O.; Rathilal, S.: Membrane technologies in wastewater treatment: a review. Membranes **10**, 89 (2020). https://doi.org/10.3390/MEMBRANES10050089
15. Ameta, R.; Solanki, M.S.; Benjamin, S.; Ameta, S.C.: Chapter 6-Photocatalysis. Advanced Oxidation Processes for Wastewater Treatment, Emerging Green Chemical Technology, p. 135–175. Academic Press, Cambridge (2018)
16. Lee, D.E.; Kim, M.K.; Danish, M.; Jo, W.K.: State-of-the-art review on photocatalysis for efficient wastewater treatment: attractive approach in photocatalyst design and parameters affecting the photocatalytic degradation. Catal. Commun. (2023). https://doi.org/10.1016/j.catcom.2023.106764

17. Lin, Y.; Li, J.; Chen, S.; Zhou, H.; Shu, Y.; Tang, L.; Long, Q.; Zhang, P.; Huang, Y.: In situ construction of pyrite-marcasite-magnetite composite via FeS_2 phase transformation and oxidation for the synergistic degradation of methyl orange and Cr(VI). Sep. Purif. Technol. **308**, 122764 (2023). https://doi.org/10.1016/J.SEPPUR.2022.122764
18. Wang, J.; Wang, B.; Zhang, W.; Xiao, Y.; Xu, H.; Liu, Y.; Liu, Z.; Zhang, J.; Jiang, Y.: Visible-light-driven double-shell $SnIn_4S_8/TiO_2$ heterostructure with enhanced photocatalytic activity for MO removal and Cr(VI) cleanup. Appl. Surf. Sci. **587**, 152867 (2022). https://doi.org/10.1016/J.APSUSC.2022.152867
19. Yang, Y.; Wang, G.; Deng, Q.; Ng, D.H.L.; Zhao, H.: Microwave-assisted fabrication of nanoparticulate TiO_2 microspheres for synergistic photocatalytic removal of Cr(VI) and methyl orange. ACS Appl. Mater. Interfaces **6**, 3008–3015 (2014). https://doi.org/10.1021/AM405607H/SUPPL_FILE/AM405607H_SI_001.PDF
20. Guan, J.; Long, Z.; Li, Q.; Han, J.; Du, H.; Wang, P.; Zhang, G.: Citric acid modulated preparation of CdS photocatalyst for efficient removal of Cr(VI) and methyl orange. Opt. Mater. **121**, 111604 (2021). https://doi.org/10.1016/J.OPTMAT.2021.111604
21. Ghani, U.; Hina, K.; Iqbal, M.; Irshad, M.K.; Aslam, I.; Saeed, R.; Ibrahim, M.: Kinetic and isotherms modeling of methyl orange and chromium (VI) onto hexagonal ZnO microstructures as a membrane for environmental remediation of wastewater. Chemosphere (2022). https://doi.org/10.1016/j.chemosphere.2022.136681
22. Xiang, H.; Ren, G.; Yang, X.; Xu, D.; Zhang, Z.; Wang, X.: A low-cost solvent-free method to synthesize α-Fe_2O_3 nanoparticles with applications to degrade methyl orange in photo-fenton system. Ecotoxicol. Environ. Saf. (2020). https://doi.org/10.1016/j.ecoenv.2020.110744
23. Hitam, C.N.C.; Jalil, A.A.; Izan, S.M.; Azami, M.S.; Hassim, M.H.; Chanlek, N.: The unforeseen relationship of Fe_2O_3 and ZnO on fibrous silica KCC-1 catalyst for fabricated Z-scheme extractive-photooxidative desulphurization. Powder Technol. **375**, 397–408 (2020). https://doi.org/10.1016/J.POWTEC.2020.07.114
24. Izzudin, N.M.; Jalil, A.A.; Ali, M.W.; Aziz, F.F.A.; Azami, M.S.; Hassan, N.S.; Fauzi, A.A.; Ibrahim, N.; Saravanan, R.; Hassim, M.H.: Promoting a well-dispersion of MoO_3 nanoparticles on fibrous silica catalyst via one-pot synthesis for enhanced photoredox environmental pollutants efficiency. Chemosphere **308**, 136456 (2022). https://doi.org/10.1016/J.CHEMOSPHERE.2022.136456
25. Fauzi, A.A.; Jalil, A.A.; Mohamed, M.; Triwahyono, S.; Jusoh, N.W.C.; Rahman, A.F.A.; Aziz, F.F.A.; Hassan, N.S.; Khusnun, N.F.; Tanaka, H.: Altering fiber density of cockscomb-like fibrous silica–titania catalysts for enhanced photodegradation of ibuprofen. J. Environ. Manage. **227**, 34–43 (2018). https://doi.org/10.1016/j.jenvman.2018.08.073
26. Hazril, N.I.H.; Jalil, A.A.; Aziz, F.F.A.; Hassan, N.S.; Fauzi, A.A.; Khusnun, N.F.; Izzudin, N.M.; Jusoh, N.W.C.; Teh, L.P.; Jaafar, N.F.; Rajendran, S.: Selective simultaneous photo-Fenton removal of Cr (VI) and methyl orange dye over critical raw material-free fibrous-silica irons catalyst. Sustain. Mater. Technol. **41**, e00994 (2024). https://doi.org/10.1016/J.SUSMAT.2024.E00994
27. Wan, J.; Xue, P.; Wang, R.; Liu, L.; Liu, E.; Bai, X.; Fan, J.; Hu, X.: Synergistic effects in simultaneous photocatalytic removal of Cr(VI) and tetracycline hydrochloride by Z-scheme $Co_3O_4/Ag/Bi_2WO_6$ heterojunction. Appl. Surf. Sci. **483**, 677–687 (2019). https://doi.org/10.1016/J.APSUSC.2019.03.246
28. Hu, M.; Zhao, D.; Yan, X.; Hu, X.; Zhou, M.; Shu, Y.; Liu, P.: Construction of Z-scheme heterojunction ZIF-8-decorated ZnO/SiO_2 for enhanced visible-light photocatalytic removal of organic pollutants and reduction of Cr (VI). Appl. Surf. Sci. **665**, 160321 (2024). https://doi.org/10.1016/J.APSUSC.2024.160321
29. Abdelfattah, I.; El-Shamy, A.M.: A comparative study for optimizing photocatalytic activity of TiO_2-based composites with ZrO_2, ZnO, Ta_2O_5, SnO, Fe_2O_3, and CuO additives. Sci. Rep. **14**, 1–26 (2024). https://doi.org/10.1038/S41598-024-77752-5
30. Aziz, F.F.A.; Jalil, A.A.; Hassan, N.S.; Fauzi, A.A.; Azami, M.S.: Simultaneous photocatalytic reduction of hexavalent chromium and oxidation of p-cresol over AgO decorated on fibrous silica zirconia. Environ. Pollut. (2021). https://doi.org/10.1016/J.ENVPOL.2021.117490
31. Hassan, N.S.; Jalil, A.A.; Hitam, C.N.C.; Sawal, M.H.; Rahim, M.N.S.; Hussain, I.; Jusoh, N.W.C.; Saravanan, R.; Prasetyoko, D.: Enhanced photooxidative desulphurization of dibenzothiophene over fibrous silica tantalum: influence of metal-disturbance electronic band structure. Int. J. Hydrog. Energy (2023). https://doi.org/10.1016/j.ijhydene.2022.02.008
32. Hassan, N.S.; Jalil, A.A.; Aldeen, E.M.S.; Bahari, M.; Teh, L.P.; Rajendran, S.; Jusoh, N.W.C.; Ainirazali, N.: Integrating ZnO with fibrous silica zirconia p–n heterojunction for effective photoredox of hexavalent chromium and congo red. J. Water Process Eng. (2024). https://doi.org/10.1016/j.jwpe.2024.105050
33. Yuan, Y.; Guo, R.T.; Hong, L.F.; Ji, X.Y.; Lin, Z.D.; Li, Z.S.; Pan, W.G.: A review of metal oxide-based Z-scheme heterojunction photocatalysts: actualities and developments. Mater. Today Energy **21**, 100829 (2021)
34. Xia, C.; Wang, H.; Kim, J.K.; Wang, J.: Rational design of metal oxide-based heterostructure for efficient photocatalytic and photoelectrochemical systems. Adv. Funct. Mater. **31**, 2008247 (2021)
35. Tho, N.T.M.; Ha, T.T.; Van Cuong, N.; Sreekanth, T.V.M.; Dang, P.H.: Novel n–p photocatalysts heterojunction via ZnO nanoparticles decorated $ZnCo_2O_4$ as an improved visible-light-driven decomposition of methylene blue and antimicrobial activity. Arab. J. Sci. Eng. **49**(6), 7961–7977 (2023). https://doi.org/10.1007/S13369-023-08597-9
36. Li, J.; Lu, Y.; Li, D.; Qi, F.; Yu, L.; Xia, C.: Effects of P-N and N-N heterostructures and band alignment on the performance of low-temperature solid oxide fuel cells. Int. J. Hydrog. Energy **46**, 9790–9798 (2021). https://doi.org/10.1016/J.IJHYDENE.2020.06.103
37. Che, L.; Pan, J.; Cai, K.; Cong, Y.; Lv, S.W.: The construction of p–n heterojunction for enhancing photocatalytic performance in environmental application: a review. Sep. Purif. Technol. **315**, 123708 (2023). https://doi.org/10.1016/J.SEPPUR.2023.123708
38. Ding, Y.; Zhang, J.; Yang, Y.; Long, L.; Yang, L.; Yan, L.; Kong, W.; Liu, F.; Lv, F.; Liu, J.: Fully-depleted dual P–N heterojunction with type-II band alignment and matched build-in electric field for high-efficient photocatalytic hydrogen production. Int. J. Hydrog. Energy **46**, 36069–36079 (2021). https://doi.org/10.1016/J.IJHYDENE.2021.08.175
39. Xu, D.; Sun, F.; Liu, F.; Shao, H.; He, W.; Wang, L.; Ma, Q.; Yu, W.; Yu, H.; Dong, X.: 2D Bi_2MoO_6 nanosheets immobilized on electrospun 1D $LaFeO_3$ hollow nanofibers: an efficacious direct Z-scheme p–n type heterojunction photocatalyst for removal of organic contaminants under visible-light irradiation. J. Environ. Chem. Eng. **12**, 111952 (2024). https://doi.org/10.1016/J.JECE.2024.111952
40. Xie, Y.; Xing, Z.; Sun, P.; Wu, S.; Zhang, X.; Li, Z.; Zhou, W.: $CuInS_2$ quantum dots/perylene diimide inorganic/organic P-N heterojunction nanofibers for enhanced photocatalytic performance. J. Environ. Chem. Eng. **13**, 115066 (2025). https://doi.org/10.1016/J.JECE.2024.115066
41. Wang, Y.; Wang, C.; Cheng, C.; Wu, H.; Liu, H.: Chromium removal at neutral pHs via electrochemical Cr(VI) reduction and subsequent Cr(III) adsorption with MoS_2 nanoflowers-modified graphite felt. J. Hazard. Mater. **455**, 131582 (2023). https://doi.org/10.1016/J.JHAZMAT.2023.131582
42. Jalil, A.A.; Triwahyono, S.; Razali, N.A.M.; Hairom, N.H.H.; Idris, A.; Muhid, M.N.M.; Ismail, A.; Yahaya, N.A.M.; Ahmad, N.A.L.; Dzinun, H.: Complete electrochemical dechlorination of

chlorobenzenes in the presence of various arene mediators. J. Hazard. Mater. (2010). https://doi.org/10.1016/j.jhazmat.2009.09.091
43. Qiu, J.; Tang, J.; Shen, J.; Wu, C.; Qian, M.; He, Z.; Chen, J.; Shuang, S.: Preparation of a silver electrode with a three-dimensional surface and its performance in the electrochemical reduction of carbon dioxide. Electrochim. Acta **203**, 99–108 (2016). https://doi.org/10.1016/j.electacta.2016.03.182
44. Rabah, M.A.; Girgis, N.N.: Mechanism of silver nanoparticles deposition by electrolysis and electroless methods on a graphite substrate. Int. J. Nonferrous Metall. (2022). https://doi.org/10.4236/ijnm.2022.101001
45. Das, B.R.; Jena, S.; Dhal, J.P.: Ag doped α-Fe_2O_3 nanoparticles: synthesis, characterization and application as heterogeneous photocatalyst for removal of organic dye from aqueous media without any oxidizing agents. J. Indian Chem. Soc. **98**, 100214 (2021). https://doi.org/10.1016/J.JICS.2021.100214
46. Do, B.L.; Ho, T.G.T.; Phan, H.P.; Nguyen, T.: Green fabrication of effective silver loading on fishbone-derived hydroxyapatite: a robust catalyst for 4-nitrophenol reduction. Arab. J. Sci. Eng. **50**(6), 3793–3805 (2024). https://doi.org/10.1007/S13369-024-09167-3
47. Hussain, I.; Jalil, A.A.; Mamat, C.R.; Siang, T.J.; Rahman, A.F.A.; Azami, M.S.; Adnan, R.H.: New insights on the effect of the H_2/CO ratio for enhancement of CO methanation over metal-free fibrous silica ZSM-5: Thermodynamic and mechanistic studies. Energy Convers Manag. **199**, 112056 (2019). https://doi.org/10.1016/J.ENCONMAN.2019.112056
48. Hamid, M.Y.S.; Firmansyah, M.L.; Triwahyono, S.; Jalil, A.A.; Mukti, R.R.; Febriyanti, E.; Suendo, V.; Setiabudi, H.D.; Mohamed, M.; Nabgan, W.: Oxygen vacancy-rich mesoporous silica KCC-1 for CO_2 methanation. Appl. Catal. A Gen. **532**, 86–94 (2017). https://doi.org/10.1016/J.APCATA.2016.12.023
49. Naseri, M.; Kamalianfar, A.; Naderi, E.; Hashemi, A.: The effect of Ag nanoparticles on physical and photocatalytic properties of $ZnFe_2O_4/SiO_2$ nanocomposite. J. Mol. Struct. (2020). https://doi.org/10.1016/j.molstruc.2020.127706
50. Hassan, N.S.; Jalil, A.A.; Triwahyono, S.; Khusnun, N.F.; Izan, S.M.; Kidam, K.; Johari, A.: Synergistic effect of microwave rapid heating and weak mineralizer on silica-stabilized tetragonal zirconia nanoparticles for enhanced photoactivity of Bisphenol A. J. Mol. Liq. (2018). https://doi.org/10.1016/j.molliq.2018.04.068
51. Nixon, P.D.; Vinesh, V.; Jayaseelan, E.; Magdalin, A.E.; Preeyanghaa, M.; Enoch, I.V.M.V.; Neppolian, B.; Ananthi, N.: Hydrothermal synthesis of sphere-shaped silver-based magnetic nanocomposite loaded on mesoporous KIT-5 for efficient photocatalytic degradation of tetracycline (TC). J. Porous Mater. **30**, 821–833 (2023). https://doi.org/10.1007/S10934-022-01387-Y/FIGURES/7
52. Sawal, M.H.; Jalil, A.A.; Abdullah, T.A.T.; Hassan, N.S.; Bahari, M.B.; Izzudin, N.M.; Jusoh, N.W.C.; Nagao, Y.; Aoki, K.; Chong, M.N.; Rajendran, S.: *n-n* heterojunction CdS/FST photoanode for enhanced photoelectrochemical water splitting. Int. J. Hydrog. Energy **104**, 336–343 (2025). https://doi.org/10.1016/J.IJHYDENE.2024.03.215
53. Wang, J.C.; Ren, J.; Yao, H.C.; Zhang, L.; Wang, J.S.; Zang, S.Q.; Han, L.F.; Li, Z.J.: Synergistic photocatalysis of Cr(VI) reduction and 4-Chlorophenol degradation over hydroxylated α-Fe_2O_3 under visible light irradiation. J. Hazard. Mater. **311**, 11–19 (2016). https://doi.org/10.1016/J.JHAZMAT.2016.02.055
54. Bi, Y.; Zhao, Y.; Meng, X.; Cong, H.; Gao, W.: Synthesis of Ag-functionalized α-Fe_2O_3 nanocomposites for ppb-level triethylamine detection. J. Alloys Compd. (2022). https://doi.org/10.1016/j.jallcom.2022.165264
55. Hu, C.; Guo, W.; Zhen, S.; Li, Y.; Huang, C.; Zhan, L.: Bimetallic Ag/Fe-MOG derived flake-like Ag_2O/Fe_2O_3 p–n heterojunction for efficient photodegradation organic pollutants within a wide pH range. J. Environ. Manage. **366**, 121686 (2024). https://doi.org/10.1016/J.JENVMAN.2024.121686
56. Sharma, G.; Bhogal, S.; Kumar, A.; Naushad, M.; Sharma, S.; Ahamad, T.; Stadler, F.J.: AgO/MgO/FeO@Si_3N_4 nanocomposite with robust adsorption capacity for tetracycline antibiotic removal from aqueous system. Adv. Powder Technol. (2020). https://doi.org/10.1016/j.apt.2020.09.006
57. Hassan, N.S.; Jalil, A.A.; Aldeen, E.M.S.; Bahari, M.; Teh, L.P.; Rajendran, S.; Jusoh, N.W.C.; Ainirazali, N.: Integrating ZnO with fibrous silica zirconia p–n heterojunction for effective photoredox of hexavalent chromium and congo red. J. Water Process Eng. **59**, 105050 (2024). https://doi.org/10.1016/J.JWPE.2024.105050
58. Li, Y.; Liu, Y.; Hao, Y.; Wang, X.; Liu, R.; Li, F.: Fabrication of core-shell $BiVO_4$@Fe_2O_3 heterojunctions for realizing photocatalytic hydrogen evolution via conduction band elevation. Mater. Des. **187**, 108379 (2020). https://doi.org/10.1016/J.MATDES.2019.108379
59. Kistner-Morris, J.; Shi, A.; Liu, E.; Arp, T.; Farahmand, F.; Taniguchi, T.; Watanabe, K.; Aji, V.; Lui, C.H.; Gabor, N.: Electric-field tunable type-i to type-ii band alignment transition in $MoSe_2/WS_2$ heterobilayers. Nat. Commun. **15**, 1–7 (2024). https://doi.org/10.1038/S41467-024-48321-1
60. Andrés, C.M.C.; de la Pérez Lastra, J.M.; Andrés Juan, C.; Plou, F.J.; Pérez-Lebeña, E.: Superoxide anion chemistry—its role at the core of the innate immunity. Int. J. Mol. Sci. **24**(3), 1841 (2023). https://doi.org/10.3390/IJMS24031841
61. Li, X.; Wang, Y.; Zou, J.; Dong, X.; Cheng, L.; Fu, W.; Jiang, Y.; Jiang, G.; Baig, S.A.: Efficient surface hydroxyl-to-hydroxyl radical conversion on layered double hydroxide via high-efficiency hydroxyl transformer. J. Colloid Interface Sci. **698**, 138014 (2025). https://doi.org/10.1016/J.JCIS.2025.138014
62. Padhi, M.K.; Kar, P.; Devi, N.; Nanda, B.B.; Nanda, B.: Solid waste derived nanocomposite of Ag (0) loaded Fe_2O_3-SiO_2 for solar power degradation of antibiotics. J. Mol. Liq. **368**, 120673 (2022). https://doi.org/10.1016/J.MOLLIQ.2022.120673
63. Devi, A.P.; Padhi, D.K.; Mishra, P.M.; Behera, A.K.: Bio-surfactant assisted room temperature synthesis of cubic Ag/RGO nanocomposite for enhanced photoreduction of Cr (VI) and antibacterial activity. J. Environ. Chem. Eng. **9**, 104778 (2021). https://doi.org/10.1016/J.JECE.2020.104778
64. Bavani, T.; Madhavan, J.; Prasad, S.; AlSalhi, M.S.; AlJaafreh, M.J.: A straightforward synthesis of visible light driven $BiFeO_3/AgVO_3$ nanocomposites with improved photocatalytic activity. Environ. Pollut. **269**, 116067 (2021). https://doi.org/10.1016/J.ENVPOL.2020.116067
65. Li, Y.; Liu, Z.; Wu, Y.; Chen, J.; Zhao, J.; Jin, F.; Na, P.: Carbon dots-TiO2 nanosheets composites for photoreduction of Cr(VI) under sunlight illumination: favorable role of carbon dots. Appl. Catal. B **224**, 508–517 (2018). https://doi.org/10.1016/J.APCATB.2017.10.023
66. Iqbal, R.M.A.; Akhtar, T.; Sitara, E.; Nasir, H.; Fazal, A.; Rafique, U.; Ullah, S.; Mehmood, A.: Development of Ag0.04ZrO_2/rGO heterojunction, as an efficient visible light photocatalyst for degradation of methyl orange. Sci. Rep. **12**(1), 1–12 (2022). https://doi.org/10.1038/s41598-022-16673-7
67. Li, J.; Mi, C.; Li, J.; Xu, Y.; Jia, Z.; Li, M.: The removal of MO molecules from aqueous solution by the combination of ultrasound/adsorption/photocatalysis. Ultrason. Sonochem. **15**, 949–954 (2008). https://doi.org/10.1016/J.ULTSONCH.2008.03.002
68. Jusoh, N.W.C.; Jalil, A.A.; Triwahyono, S.; Setiabudi, H.D.; Sapawe, N.; Satar, M.A.H.; Karim, A.H.; Kamarudin, N.H.N.; Jusoh, R.; Jaafar, N.F.; Salamun, N.; Efendi, J.: Sequential desilication–isomorphous substitution route to prepare mesostructured silica nanoparticles loaded with ZnO and their photocatalytic activity. Appl. Catal. A Gen. **468**, 276–287 (2013). https://doi.org/10.1016/J.APCATA.2013.09.005

69. Shang, Y.; Li, X.; Yang, Y.; Wang, N.; Zhuang, X.; Zhou, Z.: Optimized photocatalytic regeneration of adsorption-photocatalysis bifunctional composite saturated with methyl orange. J. Environ. Sci. **94**, 40–51 (2020). https://doi.org/10.1016/J.JES.2020.03.044
70. Liang, P.L.; Yuan, L.Y.; Deng, H.; Wang, X.C.; Wang, L.; Li, Z.J.; Luo, S.Z.; Shi, W.Q.: Photocatalytic reduction of uranium(VI) by magnetic $ZnFe_2O_4$ under visible light. Appl. Catal. B **267**, 118688 (2020). https://doi.org/10.1016/J.APCATB.2020.118688
71. Yao, L.; Chen, Z.; Li, J.; Shi, C.: Creation of oxygen vacancies to activate lanthanum-doped bismuth titanate nanosheets for efficient synchronous photocatalytic removal of Cr(VI) and methyl orange. J. Mol. Liq. (2020). https://doi.org/10.1016/j.molliq.2020.113613
72. Szeto, W.; Kan, C.W.; Yuen, C.W.M.; Chan, S.W.; Lam, K.H.: Effective photodegradation of methyl orange using fluidized bed reactor loaded with cross-linked chitosan embedded nano-CdS photocatalyst. Int. J. Chem. Eng. (2014). https://doi.org/10.1155/2014/270946
73. Dai, N.; Yi, S.; Zhang, X.; Feng, L.; Ding, H.; Song, D.; Liu, X.; Rao, J.; Zhang, Y.: Typical synthesis of an iron-modified Laponite @diatomite composite for photo-Fenton degradation of methyl orange dyes. Appl. Surf. Sci. **607**, 154886 (2023). https://doi.org/10.1016/J.APSUSC.2022.154886
74. Wang, Y.; Jia, S.; Ding, S.; Zhang, W.; Shu, R.; Hu, Y.: Development of palygorskite-$CaIn_2S_4$ composite for rapid Cr(VI) reduction under visible light. J. Environ. Sci. **156**, 562–575 (2025). https://doi.org/10.1016/J.JES.2025.02.021
75. Jangra, S.; Raza, A.; Kumar, B.; Sharma, J.; Das, S.; Pandey, K.; Mishra, Y.K.; Goyat, M.S.: MXene decorated ZnO-tetrapod for efficient degradation of Methyl Orange, Methylene Blue, and Rhodamine B dyes. Mater. Sci. Eng. B **311**, 117832 (2025). https://doi.org/10.1016/J.MSEB.2024.117832
76. Dhiman, P.; Sharma, J.; Kumar, A.; Sharma, G.; Dawi, E.A.: Construction of Ag/$Bi_7O_9I_3$ catalyst for photocatalytic degradation of Rhodamine B. Arab. J. Sci. Eng. **49**, 8443–8457 (2024). https://doi.org/10.1007/S13369-024-08931-9/METRICS
77. Anjum, F.; Gul, S.; Khan, M.I.; Khan, M.A.: Efficient synthesis of palladium nanoparticles using guar gum as stabilizer and their applications as catalyst in reduction reactions and degradation of azo dyes. Green Process. Synth. **9**, 63–76 (2020). https://doi.org/10.1515/GPS-2020-0008/ASSET/GRAPHIC/J_GPS-2020-0008_FIG_015.JPG
78. Kaur, J.; Mudgal, G.; Negi, A.; Tamang, J.; Singh, S.; Singh, G.B.; Bose, J.C.K.; Debnath, S.; Wadaan, M.A.; Farooq Khan, M.; Ruokolainen, J.; Kesari, K.K.: Reactive black-5, Congo red and methyl orange: chemical degradation of azo-dyes by *Agrobacterium*. Water (Switz.) **15**, 1664 (2023). https://doi.org/10.3390/W15091664/S1
79. Nakhostin Panahi, P.; Mohajer, S.; Rasoulifard, M.H.: Photocatalytic of congo red decolorization in the presence of Ag/AgCl/TiO_2 nanocomposite: optimization of process with Taguchi method. Arabian J. Sci. Eng. **46**(6), 5619–5632 (2021). https://doi.org/10.1007/S13369-020-05157-3
80. Zarei, M.; Ebadi, T.; Ramavandi, B.; Peighambardoust, S.J.: Photocatalytic decomposition of methylene blue and methyl orange dyes using pistachio biochar/$CoFe_2O_4$/Mn-Fe-LDH composite as H_2O_2 activator. Surfaces Interfaces **43**, 103571 (2023). https://doi.org/10.1016/J.SURFIN.2023.103571
81. Bokare, A.D.; Choi, W.: Advanced oxidation process based on the Cr(III)/Cr(VI) redox cycle. Environ. Sci. Technol. **45**, 9332–9338 (2011). https://doi.org/10.1021/ES2021704/SUPPL_FILE/ES2021704_SI_001.PDF
82. Li, P.; Liu, Y.; Xue, R.; Fan, X.: Magnetic retrievable Ag/AgBr/$ZnFe_2O_4$ photocatalyst for efficient removal of organic pollutant under visible light. Appl. Organomet. Chem. (2020). https://doi.org/10.1002/aoc.5548
83. Koysuren, O.; Koysuren, H.N.: Photoreduction of Cr(VI) on B4C/$AgFe_2O_4$ composite. J. Sol-Gel Sci. Technol. (2023). https://doi.org/10.1007/s10971-022-05981-z
84. Huang-Mu, L.; Devanesan, S.; Farhat, K.; Kim, W.; Sivarasan, G.: Improving the efficiency of metal ions doped Fe_2O_3 nanoparticles: photocatalyst for removal of organic dye from aqueous media. Chemosphere (2023). https://doi.org/10.1016/j.chemosphere.2023.139229
85. Yang, F.; Guo, Y.; Li, C.; Tang, D.; Jiang, H.; Wang, G.; Xuan, K.: Facile fabrication of $AgFe_1-xCuxO_2$ composite with abundant oxygen vacancies for boosted photocatalytic Cr (VI) reduction and organic pollutants degradation under visible light. Colloids Surf A Physicochem Eng Asp (2021). https://doi.org/10.1016/j.colsurfa.2021.127305
86. Jiménez-Rangel, K.; Samaniego-Benítez, J.E.; Jiménez-Flores, Y.; Lartundo-Rojas, L.; Calderón, H.A.; Garduño-Wilches, I.; García-García, A.; Mantilla, A.: G-C3N4(p)/AgCl as photocatalyst for the simultaneous removal of Cr (VI) and methylene blue under visible light irradiation. J. Photochem. Photobiol. A Chem. **448**, 115340 (2024). https://doi.org/10.1016/J.JPHOTOCHEM.2023.115340
87. Hashemzadeh, F.; Gaffarinejad, A.; Rahimi, R.: Porous p-NiO/n-Nb_2O_5 nanocomposites prepared by an EISA route with enhanced photocatalytic activity in simultaneous Cr(VI) reduction and methyl orange decolorization under visible light irradiation. J. Hazard. Mater. (2015). https://doi.org/10.1016/j.jhazmat.2014.12.038
88. Hu, C.; Chu, Y.C.; Lin, Y.R.; Yang, H.C.; Wang, K.H.: Photocatalytic dye and Cr(VI) degradation using a metal-free polymeric g-C_3N_4 synthesized from solvent-treated urea. Polymers (2019). https://doi.org/10.3390/polym11010182